International Journal of Heat and Mass Transfer 214 (2023) 124444

Contents lists available at ScienceDirect

International Journal of Heat and Mass Transfer

journal homepage: www.elsevier.com/locate/ijhmt

Importance of heat transfer in membrane extrusion process involving flow-induced crystallization

Tomas Barborik, Martin Zatloukal*

Department of Polymer Engineering, Faculty of Technology, Tomas Bata University in Zlin, Vavreckova 5669, 760 01 Zlin, Czechia

ARTICLE INFO

Article history:
Received 4 April 2023
Revised 5 June 2023
Accepted 22 June 2023
Available online 2 July 2023

Keywords:
Flat film production
Heat transfer
Polymer melt
Rheology
Flow-induced crystallization
Linear isotactic polypropylene
Energy storage membrane

ABSTRACT

In this work, a recently proposed viscoelastic non-isothermal extrusion film casting model, which accounts for flow-induced crystallization, was generalized by including heat transfer coefficient considering radiation, natural and forced convection. This variable heat transfer coefficient (HTC) based model was found to have the ability to predict the measured temperature, velocity, width and crystallization profile for process conditions typical for the production of polypropylene energy storage membranes. The difference between variable and constant HTC based models was investigated in more details by using systematic parametric study. The obtained results suggest that the use of the variable-HTC model should be preferred for polymer energy membrane production over the constant-HTC models, and flow-induced crystallization should always be included, otherwise the extrusion film casting model loses its ability to describe experimental reality. It is believed that the proposed model and the obtained results can help to understand the optimal process conditions for the production of polymer membranes for energy storage due to their use in rechargeable lithium-ion batteries and special energy storage.

1. Introduction

Extrusion film casting (EFC) is a technology for the production of semipermeable membranes for energy storage, which are increasingly important due to their use in rechargeable lithium-ion batteries and special energy storage [1–8]. In this technique, a polymer melt (typically polypropylene, PP) is extruded and stretched under high cooling conditions into a thin precursor film with a row-nucleated lamellar crystal structure (see Fig. 1) [9]. Intensification of cooling can be done by widening the air gap, increasing the draw intensity and/or using a specific device to increase cooling efficiency, such as an air-knife or cooling fans near the die. With regard to these processing conditions, basic isothermal models [10–43] may no longer apply, and more complex models that take temperature changes into account using the energy equation [44–73] should be used. One of the most challenging problems in this approach is the correct estimation of the heat transfer coefficient (HTC) to accurately determine cooling rates. The primary strategy is twofold: to set a constant HTC along the whole drawing distance [51–53,55–59,61–65,67,68,74], or to evaluate the HTC at different positions as the film approaches the chill roll [45–50,54,60,66,69–73,75]. Heat exchange from the film to the surroundings can be realized by various heat exchange mechanisms: conduction, convection, and radiation. Most studies have pointed out that heat conduction in the drawing direction can be neglected with respect to the heat convection and vice versa in the thickness direction due to the high value of Peclet number [68]. Based on simulations, Smith [52] found that, due to the poor thermal conductivity of the polymers, downstream rapid cooling on the chill roll insignificantly affects the film in the air gap. Once the film comes into contact with the chill roll, its geometry remains constant [56,75]. A similar approach is often used for viscous dissipation, which is considered negligible for film casting because the contribution to the HTC is much smaller than that due to advection [52]. The first group of studies relies on the assumption of a constant HTC, using supporting arguments from the predictions of some advanced models [69], which show that the HTC is almost uniform across the air gap except the regions adjacent to the die and the chill roll. The first trials for film casting were performed in 1989 [56] by fitting temperature profiles from an IR camera and later including crystallization on rolls [67,68]. Then, Smith [52] used two one-sided HTCs for the air gap and roll section to adequately describe the heat transfer to different ambient environments that do not take into account natural and radiation heat exchange mechanisms. Sollogoub et al. [58,59] performed calculations with a uniform constant HTC and based on the work of Smith et al. [53] (which showed that the HTC can vary across the

* Corresponding author.
E-mail address: mzatloukal@utb.cz (M. Zatloukal).

https://doi.org/10.1016/j.ijheatmasstransfer.2023.124444

List of Symbols

A	Aspect ratio 1
A_{1-4}	Fitting parameters in the stretch function 1, K
A_{ath}	Fitting parameter in crystallization kinetics 1
A_c	Substitution in Eq. (3) of crystallinity-modulus relationship 1
a	Regression parameter in equation of heat radiation m^{-1}
B_{ath}	Fitting parameter in crystallization kinetics s
B_f	Parameter in forced convection equation 1
B_n	Parameter in natural convection equation 1
b	Dissipation term s^{-1}
$\bar{b}$	Dimensionless dissipation term 1
$\underline{\underline{c}}$	Recoverable Finger tensor 1
$\underline{\underline{c}}^{-1}$	Inverse recoverable Finger tensor 1
$\overset{\circ}{\underline{\underline{c}}}$	Jaumann (corotational) time derivative of the recoverable Finger strain tensor s^{-1}
C_p	Specific heat capacity of polymer $J{\cdot}kg^{-1}{\cdot}K^{-1}$
$C_{p,a}$	Specific heat of air $J{\cdot}kg^{-1}{\cdot}\ K^{-1}$
c_{xx}	Normal component of the recoverable Finger tensor in axial x-direction 1
c_{yy}	Normal component of the recoverable Finger tensor in transverse y-direction 1
c_{zz}	Normal component of the recoverable Finger tensor in thickness z-direction 1
$\underline{\underline{D}}$	Deformation rate tensor s^{-1}
De	Deborah number 1
DR	Draw ratio 1
$\underline{\underline{e}}_p$	Irreversible rate of strain tensor s^{-1}
E	Dimensionless take-up force 1
E_a	Flow activation energy $J{\cdot}mol^{-1}$
E_c	Fitting parameter in crystallization kinetics K
e	Half-thickness of the film at any x location m
e_0	Die half-gap (half-thickness of the film at the die exit) m
$\bar{e}$	Dimensionless half-thickness of the film at any x location 1
F	Take-up force (drawing force) N
$f,\ h,\ m$	Parameters in function describing the effect of crystallinity on relaxation time 1
G	Linear Hookean elastic modulus Pa
G_0	Lower limit of elastic modulus in Kotula function Pa
G_1	Upper limit of elastic modulus in Kotula function Pa
$G_{1,1}$	Fitting parameter in Kotula function 1
$G_{1,2}$	Fitting parameter in Kotula function $Pa{\cdot}\ s^{-1}$
g_{acc}	Gravitational acceleration $m{\cdot}\ s^{-2}$
HTC, HTC_{total}	Heat transfer coefficient $J{\cdot}\ s^{-1}{\cdot}\ K^{-1}{\cdot}m^{-2}$
h_f	Forced convection $J{\cdot}\ s^{-1}{\cdot}\ K^{-1}{\cdot}\ m^{-2}$
h_n	Natural convection $J{\cdot}\ s^{-1}{\cdot}\ K^{-1}{\cdot}\ m^{-2}$
h_r	Radiative heat transfer coefficient $J{\cdot}\ s^{-1}{\cdot}\ K^{-1}{\cdot}\ m^{-2}$
$I_{1,c}$	First invariant of recoverable Finger tensor 1
$I_{2,c}$	Second invariant of recoverable Finger tensor 1
i	Index i, noting the spatial direction 1
j	Parameter in natural convection equation 1
$K(\bar{x})$	Crystallization kinetics function 1
K_{th}	Isothermal function of crystallization kinetics s^{-1}
k	Index of summation 1
k_a	Thermal conductivity of air $J{\cdot}\ s^{-1}{\cdot}\ K^{-1}{\cdot}\ m^{-1}$
L	Half-width of the film at any x location m
L_0	Half-width of the die (half-width of the film at the die exit) m
$\bar{L}$	Dimensionless half-width of the film at any x location 1
$\dot{m}$	Mass flow rate $kg{\cdot}h^{-1}$
M_n	Number average molar mass $g{\cdot}mol^{-1}$
M_w	Mass average molar mass $g{\cdot}mol^{-1}$
N_1	First normal stress difference Pa
N_2	Second normal stress difference Pa
n	Non-linear Leonov model parameter 1
n_c	Type of crystallization growth 1
$P(\bar{x})$	Function of non-linear crystallinity evolution 1
q	Scaling exponent in Kotula function 1
q_1	Fitting parameter in Kotula function 1
q_2	Fitting parameter in Kotula function s^{-1}
R	Gas constant $J{\cdot}\ K^{-1}{\cdot}mol^{-1}$
S_F	Stretch function in FIC 1
$\dot{T}$	Rate of cooling $°C{\cdot}\ s^{-1}$
T_k	Measured temperature of the film °C, K
$\hat{T}_k$	Predicted temperature of the film °C, K
T	Melt temperature °C, K
T_a	Ambient temperature °C, K
T_{B_f}	Calculated temperature (using the given value of B_f) °C, K
$T_{HTC_{total}}$	Calculated temperature (using the given value of constant HTC_{total}) °C, K
T_{die}	Melt temperature at the die °C, K
T_m	Melting temperature of polymer °C, K
T^0_{mq}	Flow-induced equilibrium melting temperature °C, K
T_r	Reference temperature °C, K
u	Axial velocity component of the film at any x location $m{\cdot}\ s^{-1}$
$u(X)$	Chill roll speed $m{\cdot}\ s^{-1}$
u_0	Axial velocity component at the die exit $m{\cdot}\ s^{-1}$
$\bar{u}$	Dimensionless axial velocity component of the film at any x location 1
W	Elastic potential Pa
X	Take-up length (stretching distance, air gap) m
x	Position in axial x-direction m
$\bar{x}$	Dimensionless position in axial x-direction 1
x, y, z	Spatial coordinates in axial, transverse and thickness direction, respectively 1
X_c	Crystallinity content in the polymer volume 1
X_{eq}	Equilibrium level of crystallinity in the polymer volume 1
Z	Non-isothermal function of crystallization kinetics 1
Z_x, Z_y, Z_z	Substitution variables 1
$\frac{dc_{xx}}{d\bar{x}}, \frac{dc_{yy}}{d\bar{x}}, \frac{dc_{zz}}{d\bar{x}}$	Derivative of Finger tensor components with respect to dimensionless $\bar{x}$ position 1
$\frac{d\bar{u}}{d\bar{x}}, \frac{d\bar{L}}{d\bar{x}}, \frac{d\bar{e}}{d\bar{x}}$	Derivative of dimensionless axial velocity, width and thickness with respect to dimensionless $\bar{x}$ position 1
$\frac{dX_c}{d\bar{x}}$	Derivative of crystallinity with respect to dimensionless $\bar{x}$ position 1

$\frac{dT}{d\bar{x}}$	Derivative of temperature with respect to dimensionless $\bar{x}$ position °C

Greek Symbols

α_T	Arrhenius law parameter 1
β	Non-linear Leonov model parameter 1
β_a	Volumetric expansion coefficient of air $°C^{-1}$, K^{-1}
β_{X_c}	Effect of crystallinity on elastic modulus function 1
ΔH	Crystallization latent heat $kJ{\cdot}kg^{-1}$
δ	Upper limit of summation, number of measured points 1
$\underline{\underline{\delta}}$	Unit tensor (Kronecker delta) 1
ε	Emissivity of the polymer 1
θ	Upper limit of summation, number of calculated points 1
κ_1	Fitting parameter in crystallization kinetics s^{-1}
κ_2	Fitting parameter in crystallization kinetics 1
λ	Melt relaxation time s
λ_0, λ_{die}	Melt relaxation time at the die exit s
μ_a	Dynamic viscosity of air Pa·s
ν	Non-linear Leonov model parameter 1
ν_a	Kinematic viscosity of air $m^2{\cdot}\ s^{-1}$
ξ	Non-linear Leonov model parameter 1
ξ_c	Critical relative crystallinity in Kotula function 1
$\xi_{c,1}$	Fitting parameter in Kotula function 1
$\xi_{c,2}$	Fitting parameter in Kotula function s^{-1}
ρ_a	Density of air $kg{\cdot}\ m^{-3}$
ρ_p	Polymer density $kg{\cdot}\ m^{-3}$
σ	Stefan–Boltzmann constant $J{\cdot}\ s^{-1}{\cdot}\ m^{-2}{\cdot}\ K^{-4}$
$\underline{\underline{\tau}}$	Extra stress tensor Pa
τ_{ii}	Normal stress in corresponding spatial direction Pa
$\bar{\tau}_{ii}$	Dimensionless normal stress in corresponding spatial direction 1

Latin

EFC	Extrusion film casting –
FIC	Flow-induced crystallization –
iPP, *PP*	Material: isotactic polypropylene –
PDI	Polydispersity index 1
nRSME, $nRSME_{Bf}$	Normalized root-mean-square error 1

film width due to the complex relationship between convection, radiation and lateral air stream) applied an heterogeneous heat transfer, higher at the border than in the rest of the film. However, the predictive ability of constant HTC models appears to depend on the specific cooling conditions in the air gap, and simplified models can still provide a framework for investigating the influence of thermal effects without necessarily providing quantitative predictions [57].

The second category of works deals with the evaluated HTC, which generally takes into account the following three key contributions: forced convection, natural/free convection and radiation varying along the drawing distance. Detailed early analyses of heat transfer in the air gap were given by Barq et al. [69] and for a roll section by Cotto et al. [56], Duffo et al. [68], and Billon et al. [75]. Natural convection [71] or radiation [54,66] or even forced convection together with radiation [45] were typically neglected in the early stage of non-isothermal EFC modeling to reduce computational complexity.

Lamberti et al. [72,73], in 2001, was the first to incorporate temperature induced crystallization in the EFC model. The forced convection term was modified to adopt local velocity as suggested by Duffo et al. [68], and natural convection was described by a well-known formula [76], while the radiation term was used from Barq

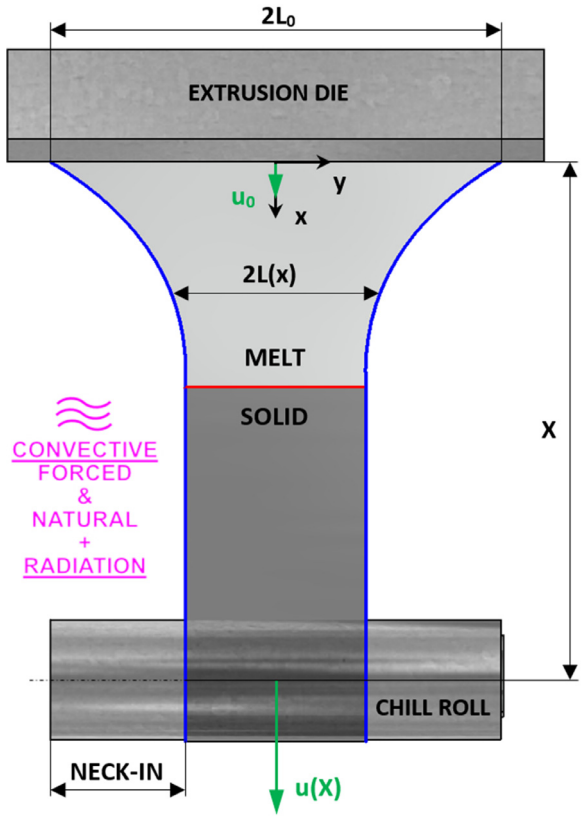

Fig. 1. Schematic representation of the extrusion film casting process.

et al. [39,69]. This approach of calculating the HTC calculation approach was adopted in the later works of Aniunoh [60], Zhou et al. [50] and Barot and Rao [47]. This study was also the inspiration for Pol et al. [48], who used a slightly different approach to calculate the forced convection term related to the film velocity, which consists of two components: the actual axial local velocity with the chill roll velocity added, similar to it is used by Barq et al. [69] and later followed by the work of Chikhalikar et al. [49].

Lamberti et al. [46], in 2005, followed up on the subject of his previous work [72] and assumed that the originally proposed model could predict the main features of the experimental temperature profiles; however, in the area near the extrusion die, the overall HTC was overpredicted. It is worth noting that the die region is critical for film formation, as most of the deformation is done here. Therefore, the forced convection term was reevaluated, and the characteristic dimension originally expressed as air gap length was replaced by the local position with the modified coefficient. In addition, radiation heat exchange was extended to include radiation from the hot metal die toward the polymer film and from the polymer film to the ambient air.

Despite the relatively large number studies that have been performed on non-isothermal EFC modeling, there is currently no physical model, that accounts for flow-induced crystallization [77]. It is therefore not surprising that our current understanding of the role of forced convection and flow-induced crystallization in EFC on the flow stability and resulting precursor film crystallinity is still rather limited. This significantly limits material and process optimization in the production of polypropylene membranes for energy storage. To fill the given knowledge gap, we have recently been the first to propose and validated a non-isothermal viscoelastic EFC model considering flow-induced crystallization [74]. However, in order to reduce the complexity of the model, a simplifying assumption considering a constant value of the HTC was used,

which may reduce the ability of the model to describe the heat transfer in EFC under processing conditions typical for the production of polymeric energy storage membranes, i.e., under very rapid cooling conditions that account for radiation, natural and forced convection, where flow-induced crystallization occurs. The aim of this work is to generalize our recently proposed EFC model by including of radiation, natural and forced convection, validate it and clarify the role of forced convection during EFC conditions typical for the production of PP membranes for energy storage. Particular attention has been paid to understanding EFC conditions in which the widely used assumption of a constant HTC does not provide realistic predictions.

2. . Mathematical modelling

2.1. Extrusion film casting (EFC) model

In this study, a viscoelastic non-isothermal EFC model utilizing 1.5-dimensional kinematics [15,78] was used and numerically solved to determine the basic process quantities in free surface flow in the region behind the die (see Fig. 1). The EFC model consists of continuity and momentum conservation governing equations, which are solved simultaneously with the embedded energy equation and the viscoelastic single-mode modified Leonov model as a constitutive equation. A detailed derivation of the EFC model and the numerical scheme used to solve it can be found in our previous studies [51,74]. In the following sections, the basic equations of the EFC model are carefully presented together with a new definition of the HTC taking into account radiation, natural and forced convection. The EFC model using a variable and constant HTC is referred to here as the "full model" and the "simplified model", respectively.

2.2. Constitutive equation and kinematics

2.2.1. Constitutive equation

The modified Leonov constitutive equation used is based on heuristic thermodynamic arguments arising from the rubber elasticity theory [79–84]. In this constitutive equation, the fading memory of a melt is determined by an irreversible dissipation process governed by the dissipation term, b. It applies the stress to the elastic strain stored in a given viscoelastic fluid according to the following formula

$$\underline{\underline{\tau}} = 2\left(\underline{\underline{c}} \cdot \frac{\partial W}{\partial I_{1,c}} - \underline{\underline{c}}^{-1} \cdot \frac{\partial W}{\partial I_{2,c}}\right) \tag{1}$$

where is the stress, and W, the elastic potential that depends on invariants $I_{1,c}$ and $I_{2,c}$ of the recoverable Finger tensor $\underline{\underline{c}}$,

$$W = \frac{3G}{2(n+1)}\left\{[1-\beta]\cdot\left[\left(\frac{I_{1,c}}{3}\right)^{n+1} - 1\right] + \beta\left[\left(\frac{I_{2,c}}{3}\right)^{n+1} - 1\right]\right\} \tag{2}$$

where G denotes a linear Hookean elastic modulus, and n are numerical parameters. The crystallinity-modulus relationship is described using a suspension model developed by Kotula and Migler [85] and generalized by Barborik and Zatloukal [74], which allows the determination of an effective elastic modulus G for a crystalizing polymer melt at a given crystalline volume fraction, X_c, by following expression

$$(1-X_c)\frac{(G_0)^{1/q} - (G)^{1/q}}{(G_0)^{1/q} + A(G)^{1/q}} + X_c\frac{(G_1)^{1/q} - (G)^{1/q}}{(G_1)^{1/q} + A_c(G)^{1/q}} = 0; A_c = \frac{1-\xi_c}{\xi_c} \tag{3}$$

where the fully crystallized solid phase and amorphous polymer melt modulus is denoted by G_1 and G_0, respectively, ξ_c is the critical percolation fraction at which the modulus begins to grow dramatically and q determines the sensitivity of the modulus at the critical percolation fraction. In the generalized version of the suspension model [74], the model parameters G_1, q, and ξ_c change with the relaxation time of the polymer melt using a power-law expressions given by Eq. (4) along with its six fixed parameters, namely $G_{1,1}$, $G_{1,2}$, q_1, q_2, $\xi_{c,1}$, and $\xi_{c,2}$ that must identified on the relevant experimental data.

$$G_1 = G_{1,2}\lambda^{G_{1,1}}; q = q_2\lambda^{q_1}; \xi_c = \xi_{c,2}\lambda^{\xi_{c,1}} \tag{4}$$

This makes it possible to include the experimentally observed feature observed by Pantani et al. [86] that the modulus of longer chains shows a higher increase with increased crystallinity compared to shorter chains. The fading memory of the liquid is determined by an irreversible dissipation process governed by the dissipation term, b, as proposed in [87] with the Mooney potential (i.e. $n = 0$ in Eq. (2)) as follows

$$b\left(I_{1,c}\right) = \frac{1}{4\lambda}\left\{\exp\left[-\xi\sqrt{I_{1,c}-3}\right] + \frac{\sinh\left[\nu\left(I_{1,c}-3\right)\right]}{\nu\left(I_{1,c}-3\right)+1}\right\} \tag{5}$$

where β and n are numerical parameters, and ξ and ν are temperature-independent adjustable model parameters. The temperature dependence of the melt relaxation time, λ, is described here by the Arrhenius form with a constant activation energy as follows

$$\lambda = \lambda_0 \exp\left[\frac{E_a}{R}\left(\frac{1}{T} - \frac{1}{T_r}\right)\right] \tag{6}$$

with $T(x)$ is the melt, respectively, E_a is the flow activation energy, λ_0 is the relaxation time of the melt at the die exit, R is the universal gas constant and T_r is the reference melt temperature.

In addition to the previous effect, the relaxation time is also influenced by the degree of crystallization. To account for this feature, the S-shaped function $\beta_{Xc}(X_c)$ that acts directly on the initial melt relaxation time λ_0 was used as follows:

$$\lambda = \beta_{X_c}(X_c)\lambda_0 \tag{7}$$

$$\beta_{X_c}(X_c) = 1 + f\exp\left(-\frac{h}{X_c^m}\right) \tag{8}$$

where f, h, m are material constants related to crystallinity. This approach was originally utilized by Titomanlio [88] for the elastic modulus, and Pantani et al. [86,89] extended it to the relaxation time. Leonov hypothesized that the dissipative process acts to create an irreversible rate of strain $\underline{\underline{e}}_p$, which in turn spontaneously reduces the rate of elastic strain accumulation as

$$\underline{\underline{e}}_p = b\left[\underline{\underline{c}} - \frac{I_{1,c}}{3}\underline{\underline{\delta}}\right] - b\left[\underline{\underline{c}}^{-1} - \frac{I_{2,c}}{3}\underline{\underline{\delta}}\right] \tag{9}$$

here, is the unit tensor and the actual recoverable elastic strain tensor $\underline{\underline{c}}$ is related to the deformation rate tensor $\underline{\underline{D}}$ as follows

$$\overset{\circ}{\underline{\underline{c}}} - \underline{\underline{c}}\cdot\underline{\underline{D}} - \underline{\underline{D}}\cdot\underline{\underline{c}} + 2\underline{\underline{c}}\cdot\underline{\underline{e}}_p = 0 \tag{10}$$

where $\overset{\circ}{\underline{\underline{c}}}$ is the Jaumann (corotational) time derivative of the recoverable Finger strain tensor.

2.2.2. Kinematics

The following paragraphs present the basic set of dimensionless equations describing the kinematics of the EFC process obtained by combining the modified Leonov constitutive equation with the continuity and momentum conservation equations, the

full in-depth derivation of which can be found in our previous work [23].

The dimensionless conversion was implemented as follows, keeping the notational convention consistent with the open literature [15]: $\bar{\tau}_{ii}$ is the component ii of the extra stress tensor (Eq. (11)), $\bar{x}$ is the axial position in the air gap, $\bar{u}$ is the axial velocity of the film, $\bar{e}$ and $\bar{L}$ are half-thickness and half-width of the film (Eq. (12)), respectively. The film drawing intensity is characterized by the draw ratio, DR, and dimensionless drawing force E, melt elasticity by the Deborah number, De, and the basic process geometry by the aspect ratio, A, (Eq. (13)).

$$\bar{\tau}_{ii} = \frac{\tau_{ii} e_0 L_0}{F} \tag{11}$$

$$\bar{x} = \frac{x}{X}; \bar{u} = \frac{u}{u_0}; \bar{e} = \frac{e}{e_0}; \bar{L} = \frac{L}{L_0} \tag{12}$$

$$DR = \frac{u(X)}{u_0}; \frac{1}{E} = \frac{FX}{G\lambda e_0 L_0 u_0}; De = \frac{\lambda u_0}{X}; A = \frac{X}{L_0} \tag{13}$$

In the given equations, F is the drawing force acting on the film, X is the length of the air gap, x is any given position in the air gap.

Using the Mooney potential in the modified Leonov constitutive equation (i.e. when $n = 0$ and $\beta \neq 0$ in Eq. (2)), the relationship between the dimensionless stress and the recoverable strain is given by Eq. (14). The diagonal components of the recoverable strain tensor, c_{ii} , and their derivatives with respect to $\bar{x}$ are then expressed via Eqs. (15)–17.

$$\bar{\tau}_{ii} = \frac{E}{De} c_{ii} - \frac{E}{De} c_{ii} \cdot \beta - \frac{E}{De} c_{ii}^{-1} \cdot \beta \tag{14}$$

$$\frac{dc_{xx}}{d\bar{x}} = 2c_{xx} \frac{1}{\bar{u}} \frac{d\bar{u}}{d\bar{x}} - \frac{2\bar{b}}{\bar{u}} Z_x \tag{15}$$

$$\frac{dc_{yy}}{d\bar{x}} = 2c_{yy} \frac{1}{\bar{L}} \frac{d\bar{L}}{d\bar{x}} - \frac{2\bar{b}}{\bar{u}} Z_y \tag{16}$$

$$\frac{dc_{zz}}{d\bar{x}} = 2c_{zz} \frac{1}{\bar{e}} \frac{d\bar{e}}{d\bar{x}} - \frac{2\bar{b}}{\bar{u}} Z_z \tag{17}$$

The dimensionless streamwise strain rate, $d\bar{u}/d\bar{x}$, is defined in Eq. (18), while the dimensionless half-width, $d\bar{L}/d\bar{x}$, and half-thickness, $d\bar{e}/d\bar{x}$, strain rates are calculated according to Eqs. (19) and (20), respectively.

$$\frac{d\bar{u}}{d\bar{x}} = \frac{\bar{b}[\beta(Z_x - Z_z) - Z_x + Z_z] + \bar{b}\beta\left(\frac{1}{c_{zz}^2} Z_z - \frac{1}{c_{xx}^2} Z_x\right) + \frac{\bar{u}}{\bar{L}} \frac{d\bar{L}}{d\bar{x}} \left(c_{zz}(1-\beta) + \frac{\beta}{c_{zz}}\right)}{\beta(c_{xx} + c_{zz}) - c_{xx} - c_{zz} - \frac{\beta}{c_{xx}} \left(\frac{c_{zz} + c_{xx}}{c_{zz}}\right) + \frac{De\bar{u}}{2E}} \tag{18}$$

$$\frac{d\bar{L}}{d\bar{x}} = -A\sqrt{\frac{\bar{\tau}_{yy} - \bar{\tau}_{zz}}{\bar{\tau}_{xx} - \bar{\tau}_{zz}}} \tag{19}$$

$$\frac{d\bar{e}}{d\bar{x}} = -\left(\frac{1}{\bar{L}} \frac{d\bar{L}}{d\bar{x}} + \frac{1}{\bar{u}} \frac{d\bar{u}}{d\bar{x}}\right)\bar{e} \tag{20}$$

where $\bar{b}$ and Z_i are given as follows

$$\bar{b} = \frac{X}{u_0} b; Z_i = c_{ii}\left[c_{ii} - c_{ii}^{-1} + \frac{1}{3}\left(c_{xx}^{-1} + c_{yy}^{-1} + c_{zz}^{-1} - c_{xx} - c_{yy} - c_{zz}\right)\right] \tag{21}$$

2.3. Energy equation

The energy balance equation [72] used in this study gives the change in temperature, crystallinity, including flow-induced crystallization with a variable the HTC to capture the total heat exchange with the environment is defined as follows:

$$\frac{dT}{d\bar{x}} = \frac{2HTC_{total}(T_a - T)\bar{L}X}{C_p \dot{m}} + \frac{\Delta H}{C_p} \frac{dX_c}{d\bar{x}} \tag{22}$$

where $\bar{L}(x)$ is dimensionless half-width of the film, X is the length of the air gap, $\bar{x}$ is the dimensionless position within the air gap, HTC_{total} is the overall heat transfer coefficient, C_p is the specific heat capacity, $\dot{m}$ is the mass flow rate in quarter-cross-section, ΔH is the latent heat of crystallization, $T(x)$ and T_a are the melt and the ambient air temperature, respectively, $X_c(x)$ denotes the crystalline volume fraction in the polymer.

2.3.1. Heat transfer coefficient

The overall heat transfer coefficient, HTC_{total}, is not considered a constant in the air gap [51], but it is calculated more realistically to describe the complex heat exchange with surroundings by the following three different mechanisms; forced, h_f, and natural convection, h_n, and heat transfer by radiation, h_r:

$$HTC_{total}(x) = h_f + h_n + h_r \tag{23}$$

The sum of these contributors expresses the total heat exchange with the surrounding environment. For forced convection, a thin plate/film in the air stream is assumed using the local velocity formula taken from [68], and the characteristic dimension is taken as the inverse of the true position in the air gap [46] originating from [69].

$$h_f = B_f \frac{k_a}{(X - x)} \left[\frac{u(X - x)\rho_a}{\mu_a}\right]^{0.5} \left[\frac{C_{p,a}\mu_a}{k_a}\right]^{0.33} \tag{24}$$

where B_f is the forced convection parameter, k_a is the thermal conductivity of the air, ρ_a is the air density, μ_a is the dynamic viscosity of the air, $C_{p,a}$ is the specific heat capacity of the air and x is the position in the air gap . The natural convection term was evaluated according to the following formula [76]

$$h_n = B_n \frac{k_a}{X} \left[\frac{g_{acc}\beta_a X^3 (T - T_a)}{\nu_a^2} \frac{C_{p,a}\mu_a}{k_a}\right]^j \tag{25}$$

where B_n and j are the natural convection parameters, g_{acc} is the gravitational acceleration, β_a is the volumetric expansion coefficient of air and ν_a is the kinematic air viscosity. Based on the Stefan-Boltzmann law, the contribution to radiative heat transfer is described as

$$h_r = \varepsilon(e)\sigma \frac{T_a^4 - T^4}{T_a - T} \tag{26}$$

where ε and σ are denoted as the emissivity of the polymer and the Stefan–Boltzmann constant, respectively, and $e(x)$ is the half-width of the film. An important role is played by the emissivity, which is a function of the film thickness using the following formula [72]

$$\varepsilon(e) = 1 - \exp(-ae) \tag{27}$$

here a is the regression parameter that was evaluated as 2662 m^{-1} for iPP films [39,90].

2.3.2. Crystallization kinetics

The crystallization kinetics model used in this study was originally drawn by Ziabicki [91,92] and later modified by Lamberti [93]. The resulting semi-dimensionless form of the crystallinity evolution equation, X_c, in the spatial coordinates is given as

$$\frac{dX_c(\bar{x})}{d\bar{x}} = X_{eq} \exp\left\{-[P(\bar{x})]^{n_c}\right\} n_c [P(\bar{x})]^{n_c-1} \frac{dP(\bar{x})}{d\bar{x}} \frac{X}{\bar{u}u_0} \tag{28}$$

where X_{eq} is the equilibrium volume content of crystallinity (the maximum in the crystalline phase that the melt can contain), the constant n_c has a value of 3 to capture heterogeneous nucleation and three-dimensional crystal growth [92], and $\bar{u}(x)$ and u_0 are the dimensionless axial and initial film velocities. The function expressing the nonlinear description of crystallinity development is denoted as $P(\bar{x})$:

$$K(\bar{x}) = \frac{d}{d\bar{x}} P(\bar{x}) \bar{u} u_0 X \tag{29}$$

Here, $K(\bar{x})$ is the overall crystallization kinetics factor characterizing the rate of crystallization:

$$K = K_{th}\left(1 + \frac{dT}{d\bar{x}} \bar{u} u_0 X Z\right)^{1/n_c} \tag{30}$$

in which the effect of temperature on crystallization is captured by functions K_{th} as follows

$$K_{th} = \kappa_1 \frac{T(T_m - T)}{(T_m)^2} \exp\left[-\frac{E_c}{RT}\right] \exp\left[-\kappa_2 \frac{(T_m)^2}{T(T_m - T)}\right] \tag{31}$$

where κ_1, κ_2, and E_c are material parameters determined from the isothermal test, R is the universal gas constant. The influence of the cooling rate on the crystallization kinetics is, on the other hand, covered by the non-isothermal function, Z, of the form

$$Z = -B_{ath} \left|\dot{T}\right|^{A_{ath}} \frac{(T_m)^5}{T(T_m - T)^5} \exp\left[\frac{E_c}{RT}\right] \tag{32}$$

$$\dot{T} = \bar{u} u_0 X \frac{dT}{d\bar{x}} \tag{33}$$

where, the cooling rate is denoted as $\dot{T}$, B_{ath} and A_{ath} are the material parameters introduced by Lamberti and Titomanlio [93] to improve the ability of the model to describe the crystallinity evolution at very high cooling rates. Finally, T and T_m are instantaneous and the melting temperature of the polymer, respectively. The fitting parameters κ_1, κ_2, E_c, B_{ath}, and A_{ath} for the material used in this work were determined in [93].

2.3.3. Flow-induced crystallization

The effect of flow on crystallization kinetics follows the concept that molecular strain causes a decrease in the melt entropy, which increases the melting temperature [94] as follows

$$T_m(S_F) = \frac{1}{2}\left[\tanh\left(\frac{S_F - A_1}{A_2}\right) + 1\right](A_3 S_F + A_4) + T^0_{mq} \tag{34}$$

where T^0_{mq} and $T_m(S_F)$ are the equilibrium and quiescent melting temperature, A_{1-4} are the experimentally determined parameters, and S_F is the molecular stretch function using the first invariant of recoverable Finger tensor $I_{1,c}$:

$$S_F = I_{1,c} - 3 \tag{35}$$

2.4. Numerical solution methods

The improved film casting model consisting of a set of first-order ordinary differential equations was solved with a 4th order Runge-Kutta method with adaptive step-size control. For more precise control over the calculation steps, the solver was developed in C++ with the results passed to GNUPLOT for visualization purposes. Due to the geometric symmetry of the film, only 1/4 of the film cross-section was used in the calculation, as showed in [70]. The computation begins with a data loading and preprocessing phase in which the implicit Kotula's function Eq. (3)) is iteratively precomputed for later facilitated utilization to determine the elastic modulus of the crystallizing melt. An initial estimate of the drawing force is then made based on the current value of the relaxation time at the die exit. It is worth noting that the drawing force increases by order of magnitude with the relaxation time, and its initial satisfactory estimation contributes to numerical stability and induces shorter computation times (the drawing force values correspond to low draw ratios, just above the unity, usually requiring a shorter Runge-Kutta method step calculation, which results in significantly longer calculation time). The preparatory phase is completed by the iterative calculation of the stress boundary conditions, followed by the solution of the main set of eight differential equations for the crystallization kinetics (Eq. (28)), the energy of equation (Eq. (22)), the half-width of the film (Eq. (19)), the axial velocity (Eq. (18)), the half film thickness (Eq. (20)), the components of the recoverable elastic strain tensor (Eqs. (15)–((17)) for each Runge-Kutta method step in which the current melting temperature of the polymer is estimated using Eq. (34) to reflect flow-induced crystallization effects. The main change in the updated calculation scheme lies in the core calculation block, more specifically in the part where the energy equation is solved, see Fig. 2. While the original approach relied on a single constant value of heat transfer coefficient, HTC, Eq. (23), used in each calculation step, the new/revised concept is designed to evaluate HTC in terms of radiation, Eq. (26), natural, Eq. (25), and forced convection, Eq. (24), based on the actual die-roll position, film axial velocity, temperature, and thickness to better describe the experimental reality. The main set of equations is repeatedly solved according to the step size of the Runge-Kutta method until the position of the chill rolls, i.e. position $\bar{x} = 1$, is reached. Depending on whether the desired draw ratio is achieved at the chill rolls, the initially estimated drawing force is iteratively updated (increased or decreased) for each subsequent calculation until convergence using the bisection method. After the calculation task is completed, the calculated data was subsequently processed for analytical purposes. The typical computation time for evaluating one prescribed DR... is about 6 min on a PC with an Intel Core i7–7700 CPU, 32 GB DDR4 RAM, and an NVMe SSD without using parallelism means. More information about the basics of calculation scheme, including methods of stabilization and calculation of boundary conditions, can be found in our previous work [74].

3. Results and discussion

3.1. Model validation

In order to verify the EFC model, the experimental data taken from the work of G. Lamberti and G. Titomanlio ([95] and [96]) for linear isotactic polypropylene (iPP) was used. Their film casting experiments were performed on the laboratory scale extruder with an additional take-up device utilizing the sensors for online measurement of width and axial velocity (image analysis), temperature (infrared pyrometry), crystallinity (collection and analysis of FTIR transmission spectra by modified M2000 FT-IR spectrometer manufactured by Midac Co.), and orientation [95]. The quiescent kinetic experiments were performed via both DSC (Mettler DSC30) and custom-tailored apparatus designed to quench thin polymer films while crystallization kinetics was examined by analyzing the intensity of depolarized light cutting across the sample [96]. The

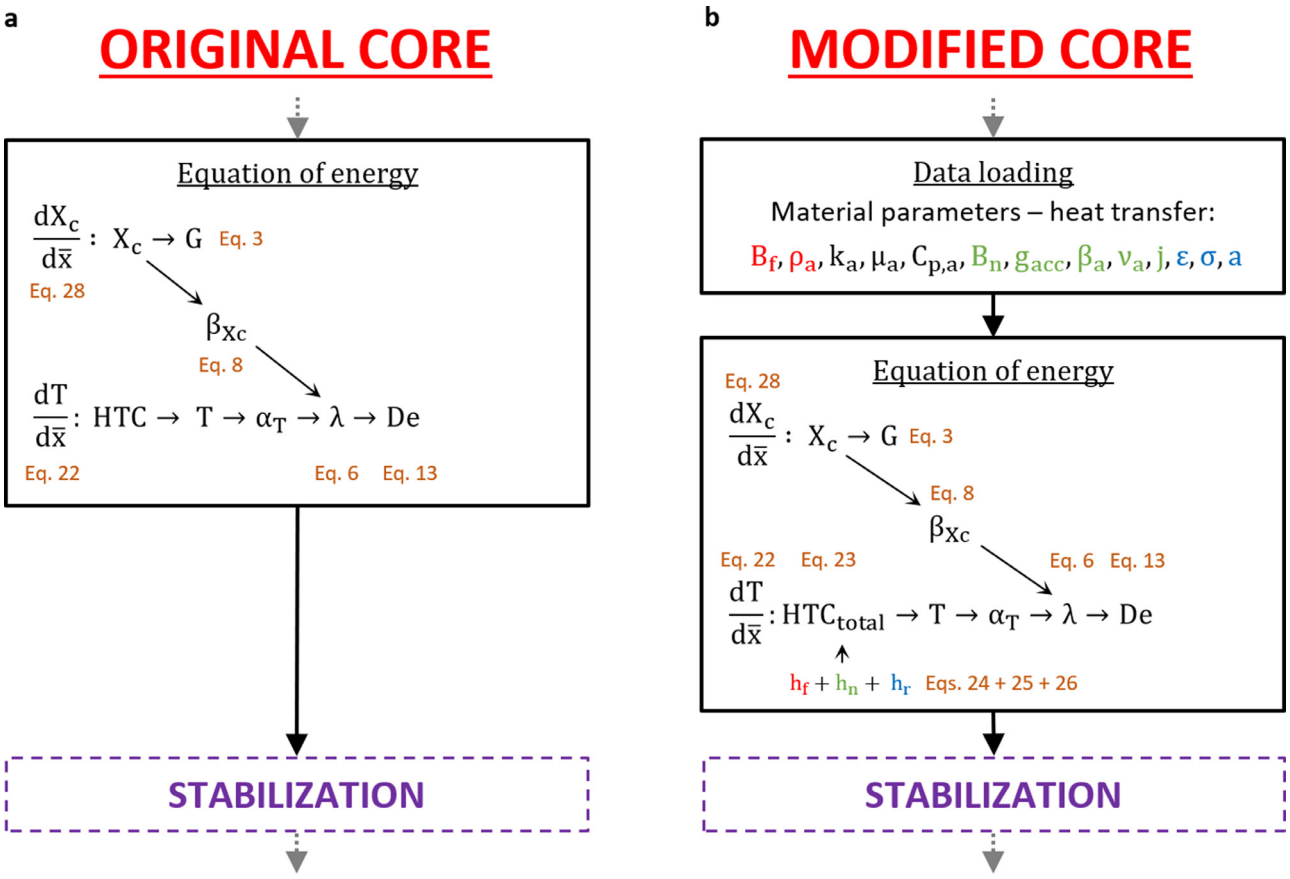

Fig. 2. Core part of calculation scheme: (a) original core, (b) modified core. The full numerical scheme is presented in our previous work [74].

Table 1
Constitutive equation parameters for iPP T30G material.

Constitutive equation			
λ(T)	**λ_0** (s)	0.1	Average melt relaxation time at the die exit (T_{die}=220°C) [99]
Eq. (6)	**E_a** (kJ·mol^{-1})	41.736	Flow activation energy [100]
	T_r (°C)	140	Reference temperature [86]
	R (J· K^{-1}·mol^{-1})	8.314	Universal gas constant
λ(X_c)	**f** (1)	1 000	Parameters in the function describing the effect of crystallinity on the relaxation time, (fitted over the experimental data set in [86] Fig. 10b therein)
Eqs. (7)–(8)	**h** (1)	1.73519	
	m (1)	0.65159	
G(X_c)	**G_0** (Pa)	45 447	Elastic modulus of the amorphous polymer melt
Eqs. (3)–(4)	**$G_{1,1}$** (1)	0.78	Generalized model parameters for the elastic modulus defined by Eq. (4) that were identified in [74] on experimental data taken from Fig. 10a in [86]
	$G_{1,2}$ (Pa· s^{-1})	900	
	q_1 (1)	10^{-4}	
	q_2 (s^{-1})	1.42	
	$\xi_{c,1}$ (1)	−0.028	
	$\xi_{c,2}$ (s^{-1})	0.165	
Modified Leonov model	**ξ** (1)	0	Non-linear Leonov model parameters [74]
Eqs. (2) and (5)	**ν** (1)	0.5	
	β (1)	0.5	

active cooling operation on the film was accomplished by a set of linear nozzles capable of blowing air on both sides of the film to facilitate film flow-induced crystallization.

In a first step, experimental data taken from [96] for linear isotactic polypropylene (iPP) performed at an extremely high cooling speed (86 °C/s) were used to validate the EFC model with respect to its ability to describe film temperature and predict crystallinity. Corresponding material and experimental conditions/parameters were taken from open literature and are listed in Tables 1-3 (process conditions marked as Ab1). The numerical scheme proposed in our previous work [74] was used to solve the EFC model. The die exit stress state is assumed to be given by a constant ratio of the second and the first normal stress difference, $-N_2/N_1$=0.2 [51,97], because the effect of the flow history inside the extrusion die can be considered negligible since the Deborah number at the exit of the die is less than 0.3 [26] for the considered processing condition. The HTC represents the only unknown that must be sufficiently defined and identified for the model to become fully predictive. In this work, two different approaches are used to include HTC in film casting modeling. In the *full model*, convection (both natural and forced) and radiation were considered to describe the total heat exchange between the film and the sur-

Table 2
Parameters of the energy and crystallization kinetics equation for iPP T30G material.

Energy equation			
Heat transfer coefficient *Eqs. (24)–(27)*	$\mathbf{k_a}$ (J· s^{-1}· K^{-1}· m^{-1})	0.0257	Thermal conductivity of air [48]
	$\boldsymbol{\rho_a}$ (kg· m^{-3})	1.2	Density of air [48]
	μ_a (10^{-5} Pa·s)	1.82	Dynamic viscosity of air [48]
	$\mathbf{C_{p,a}}$ (J·Kg^{-1}· K^{-1})	1 005	Specific heat of air [48]
	$\boldsymbol{\beta_a}$ (°C^{-1}, K^{-1})	0.0034	Volumetric expansion coefficient of air [48]
	$\mathbf{g_{acc}}$ (m· s^{-2})	9.81	Gravitational acceleration [48]
	a (m^{-1})	2 662	Regression parameter in the equation of heat radiation [46]
	$\mathbf{B_n}$ (1)	0.01	Parameter in the natural convection equation [48]
	j (1)	0.25	Parameter in the natural convection equation [48,72]
	$\boldsymbol{\sigma}$ (J· s^{-1}· m^{-2}· K^{-4})	5.67 × 10^{-8}	Stefan–Boltzmann constant [48]
Crystallization kinetics *Eqs. (28) and (30–32)*	$\mathbf{X_{eq}}$ (1)	0.61	Equilibrium level of crystallinity in the polymer volume [101]
	$\mathbf{n_c}$ (1)	3	Type of crystallization growth [101]
	$\mathbf{T_m}$ (K)	463.15	Melting temperature of the polymer [101]
	$\mathbf{E_c/R}$ (K)	45 570	Crystallization kinetics parameters taken from [101]
	$\boldsymbol{\kappa_1}$ (10^{69} s^{-1})	2.778	
	$\boldsymbol{\kappa_2}$ (1)	5.871	
	$\mathbf{A_{ath}}$ (1)	1.7721	
	$\mathbf{B_{ath}}$ (10^{-57} s)	3.448	
Flow-induced crystallization *Eq. (34)*	$\mathbf{A_1}$ (1)	1.15	Parameters of the stretch function describing the evolution of T_m taken from [94]
	$\mathbf{A_2}$ (1)	0.26	
	$\mathbf{A_3}$ (K)	1	
	$\mathbf{A_4}$ (K)	4.92	
	T^0_{mq} (°C)	190	Flow-induced equilibrium melting temperature [93]

Table 3
Summary of basic material characteristics for iPP T30G and processing conditions used.

Material and process			
Basic material characteristics	$\mathbf{M_n}$ (g·mol^{-1})	75 000	Number average molar mass [46,96]
	$\mathbf{M_w}$ (g·mol^{-1})	481 000	Mass average molar mass [46,96]
	PDI (1)	6.4	Polydispersity index [46,96]
	$\boldsymbol{\eta_0}$ at T_{die} (Pa·s)	4 545	Newtonian (zero-shear rate) viscosity, from Fig. 8 and Table II in [86]
	Tacticity (mmmm)	87.6%	Tacticity [46,96]
	$\mathbf{E_a}$ (kJ·mol^{-1})	41.736	Flow activation energy [100]
	$\mathbf{C_p}$ (J·kg^{-1}· K^{-1})	1 926	Specific heat capacity of the polymer [102]
	$\boldsymbol{\rho_p}$ (kg· m^{-3})	743.9	Polymer density, calculated from [74,103] for T_{die}
	ΔH (kJ·kg^{-1})	209	Crystallization latent heat for fully crystalline iPP [104]
Processing conditions (Ab1 | Z1 and Z2)	$\mathbf{u_0}$ (10^{-3} m· s^{-1})	4 | 4.7	Axial velocity component at the die exit [96] | [95]
	u(X) (10^{-3} m· s^{-1})	103 | 150	Chill roll speed [96] | [95]
	X (m)	0.4	Take-up length (air gap) [96]
	$\mathbf{T_{die}}$ (°C)	220	Melt temperature at the die [96]
	$\mathbf{T_a}$ (°C)	20	Ambient temperature
	$\mathbf{2L_0}$ (m)	0.2	Width of the die (width of the film at the die exit) [96]
	$\mathbf{2e_0}$ (10^{-4} m)	3 | 5	Die gap (thickness of the film at the die exit) [96] | [95]
	DR (1)	25.75[a] | 32	Draw ratio [95]

[a] The value was calculated from the values of u_0 and u(X) from [96] via Eq. (13) for DR.

roundings using Eqs. (23)–(27). In this case, the HTC depends on the actual film temperature and the position between the die and the chill roll. In the *simplified model*, the HTC given in the energy equation (Eq. (22)) is considered a constant. Independently of the type of heat transfer approach used, there is only one fitting parameter to be identified from the measured temperature profile to have a fully predictive model. Namely, a parameter of forced convection B_f, which appears in the Eq. (24) or HTC_{total} constant in Eq. (22) for full and simplified model, respectively. In order to find the parameter, its value has been systematically changed (from 0 to 50 with step 0.1) to minimize the degree of deviations between the measured and calculated temperature profile evaluated by normalized Root Mean Square Error, *nRMSE*, defined as

$$nRMSE = \sqrt{\frac{1}{\delta}\sum_{k=1}^{\delta}\left[\left(\frac{T_k(\bar{x}) - T_a}{T_{die} - T_a}\right) - \left(\frac{\hat{T}_k(\bar{x}) - T_a}{T_{die} - T_a}\right)\right]^2} \tag{36}$$

where δ is the number of measured points, $T_k(\bar{x})$ and $\hat{T}_k(\bar{x})$ represent measured and predicted temperature of the film at a given dimensionless drawing distance $\bar{x}$, T_{die} is the film temperature at the die exit and T_a is the air temperature. This procedure was applied for full and simplified model to obtain optimum values for B_f and HTC_{total}, respectively, using the EFC model accounting for flow-induced crystallization (see Fig. 3) and also when flow-induced crystallization is turned off (see Fig. 4). In these two figures, the predicted HTCs are shown along with the model predictions for film temperature and film crystallinity for both considered cases, which are compared with the corresponding measured data.

As can be seen in Fig. 3, the model accounting for flow-induced crystallization using the full model is able to nicely describe the measured temperature and crystallization profile for the given processing conditions, as the model can handle low and high (i.e. different) cooling intensity at the die exit and chill roll region, respectively. However, in the case of the simplified model, the cooling intensity remains the same, and therefore the model underestimates the temperature in the die exit region due to the high cooling intensity enhancing flow-induced crystallization, which generates exothermic heat causing the artificial formation of a local maxi-

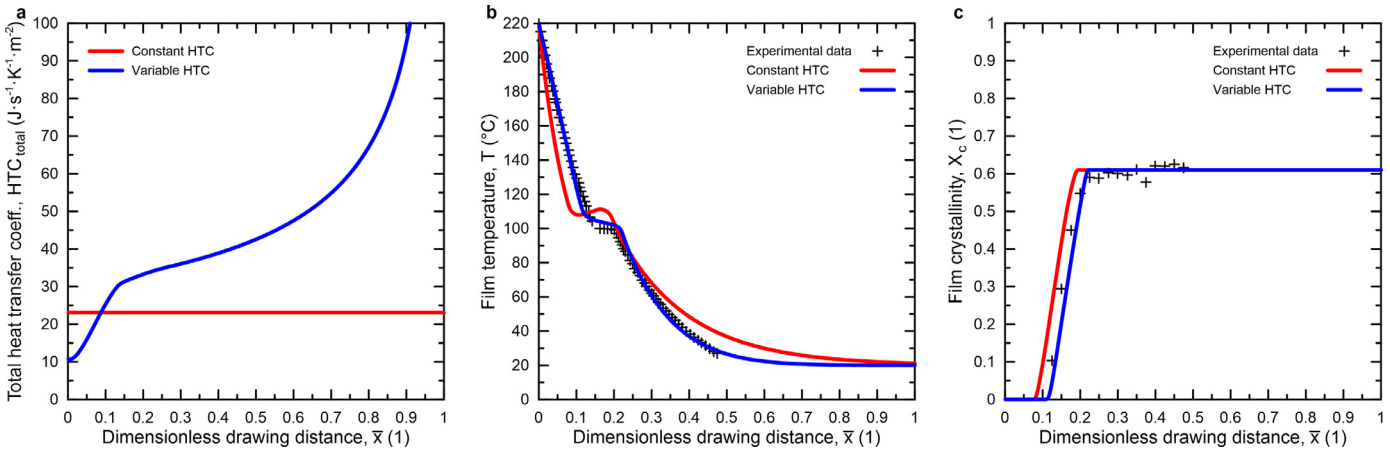

Fig. 3. Model predictions for the development of HTC_{total} (a), film temperature (b), and film crystallinity (c) as a function of dimensionless drawing distance *accounting for flow-induced crystallization* and using two different expressions for the HTC in the energy equation for process conditions summarized in Table 3 (marked as Ab1). Experimental data are taken from [96]. The model predictions are provided for optimum values of B_f=10 (full model - variable HTC approach) and HTC_{total}=23.1 J·s^{-1}·K^{-1}·m^{-2} (simplified model - constant HTC approach).

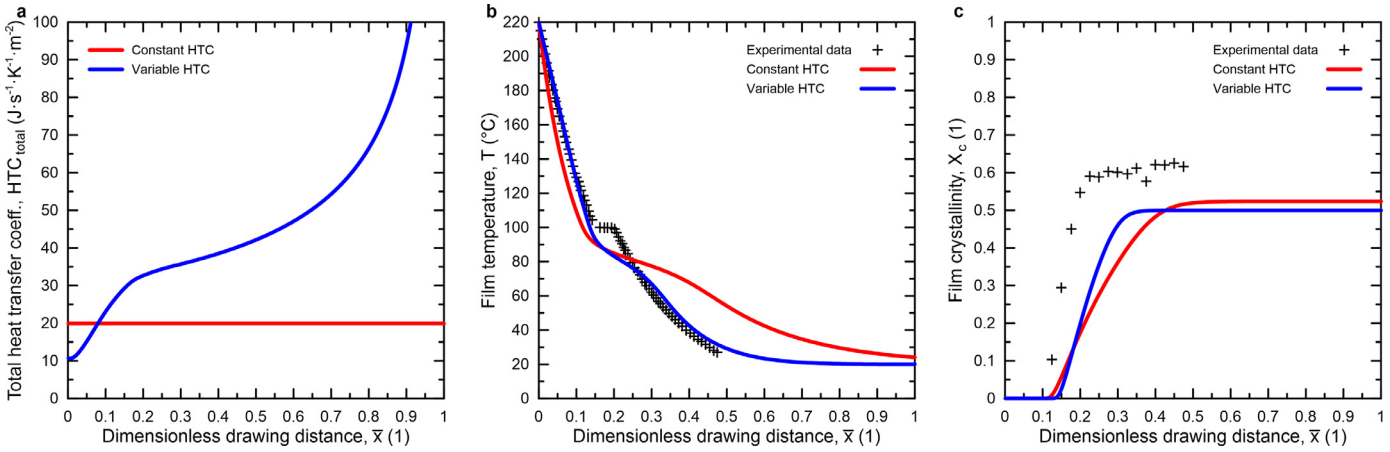

Fig. 4. Model predictions for the development of HTC_{total} (a), film temperature (b), and film crystallinity (c) as a function of dimensionless drawing distance with *flow-induced crystallization turned off* and using two different expressions for the HTC in the energy equation for process conditions summarized in Table 3 (marked as Ab1). Experimental data are taken from [96]. The model predictions are provided for optimum values of B_f=9.9 (full model - variable HTC approach) and HTC_{total}=19.9 J·s^{-1}·K^{-1}·m^{-2} (simplified model - constant HTC approach).

mum in the temperature profile. Then, the model starts to overestimate the temperature towards the direction of chill roll, because the cooling intensity is insufficient.

The effect of variable and constant HTC approach on the behavior of the model with flow-induced crystallization turned off is shown in Fig. 4. Although the variable HTC approach provides a higher ability to describe the measured temperature profile than the constant HTC approach (the reason is the same as discussed above), neither of them is able to describe the region of the temperature profile that corresponds to the onset of crystallization (the constant temperature region occurring at the dimensionless drawing distance about 0.2). It is therefore not surprising that the model with flow-induced crystallization turned off (i.e. neglecting the increase in melting temperature and crystallization rate due to the decrease in melt entropy caused by the alignment of polymer chains) underestimates the crystallinity of the film because crystallization occurs at lower temperatures (i.e. later, further from the extrusion die) and slower than when considering flow-induced crystallization (see Fig. 4c).

In a second step, experimental data taken from [95] for linear isotactic polypropylene (iPP) performed at low (experiment Z1 – blowing air off) and high (experiment Z2 – blowing air on) cooling intensities while maintaining the same operational conditions were used to further validate the EFC full model (flow-induced crystallization switched-on) with respect to its ability to describe film temperature and predict film width and velocity. Photographs for extrusion film casting experiment Z1 and Z2 are provided in Fig. 5a and Fig. 5b, respectively, and the corresponding material and processing conditions are provided in Tables 1-3. The only free parameter B_f of the EFC model that appears in Eq. (24) for forced convection, was identified for experiment Z1 and Z2 by minimizing the degree of deviation between the measured and calculated temperature profile (i.e. minimizing the *nRMSE* given by Eq. (36)), see Fig. 6a. When B_f parameter of the EFC model was available, the film velocity and width were predicted and compared with the corresponding experimental data as shown in Fig. 6b-c. It can be seen that the agreement between the model predictions and the measured data for film velocity and width is reasonable, even though the number of experimental points for the temperature profile used to identify the B_f parameter is low.

3.2. Parametric study

The objective of the parametric study is to assess the differences between EFC model using variable and constant HTC approaches at different cooling intensities for iPP and reference ex-

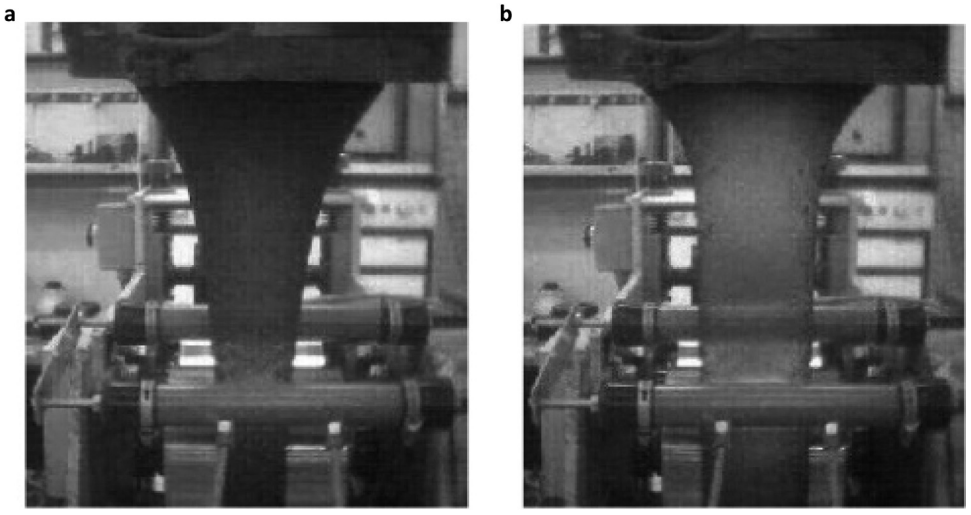

Fig. 5. Photograph of an extrusion film casting experiment for iPP T30G [95] performed under the same operating conditions summarized in Table 3 but different cooling intensities: (a) experiment Z1 – cooling air is off, (b) experiment Z2 – cooling air is on. Note that a mixture of iPP T30G with carbon black was used to better visualize producing films. Reproduced with permission from G. Lamberti, and G. Titomanlio, "Analysis of Film Casting Process: Effect of Cooling during the Path in Air," Ind. Eng. Chem. Res. 45(2), 719 (2006). Copyright 2006 American Chemical Society. (For interpretation of the references to colour in this figure legend, the reader is referred to the web version of this article.)

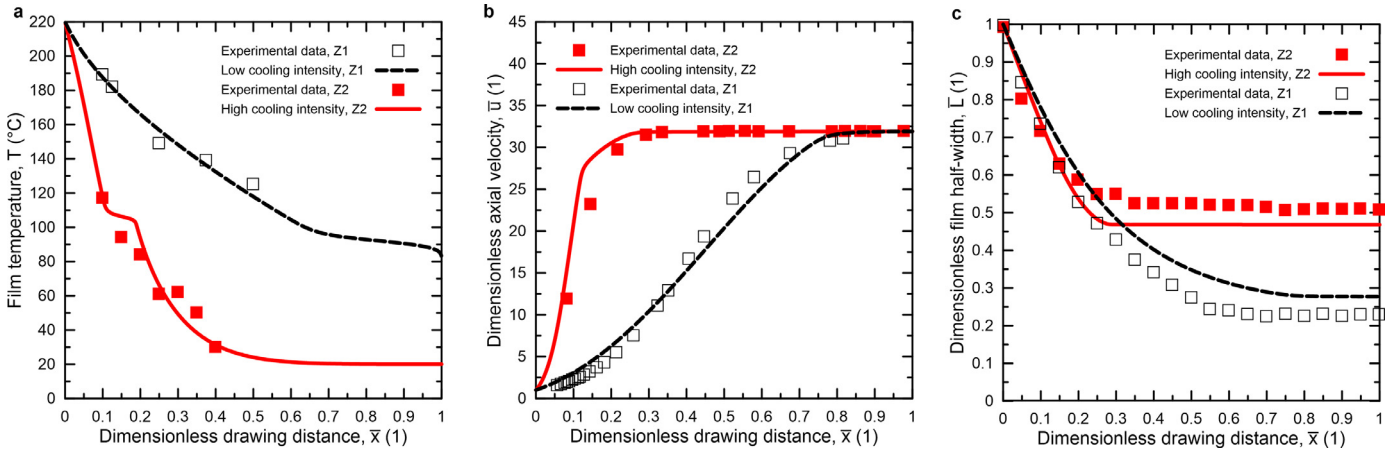

Fig. 6. Model predictions for the film temperature (a), dimensionless film axial velocity (b), and dimensionless film half-width (c) as a function of dimensionless drawing distance with *flow-induced crystallization turned on* for the same operating conditions but different cooling intensities (i.e. experiments Z1 and Z2 with processing conditions summarized in Table 3). Experimental data are taken from [95]. The model predictions are provided for optimum values of B_f=4 (case Z1) and B_f=19 (case Z2).

perimental process conditions summarized in Table 3 (marked as Ab1). The procedure was as follows. First, forced convection parameter B_f appearing in expression for variable HTC given by Eq. (24) as well as the constant HTC_{total} value were varied from 0 to 70 with step 0.01 in full and simplified models, respectively, to predict realistic values for the following key variables: temperature, crystallinity, width of the film and take-up force. Second, $nRMSE_{B_f}$ values were calculated via Eq. (37) to evaluate differences between temperature profile (i.e. dependence of the film temperature vs. dimensionless drawing distance $\bar{x}$) obtained for full and simplified model

$$nRMSE_{B_f} = \sqrt{\frac{1}{\theta}\sum_{k=1}^{\theta}\left[\left(\frac{T_{B_f,k}(\bar{x}) - T_a}{T_{die} - T_a}\right) - \left(\frac{T_{HTC_{total},k}(\bar{x}) - T_a}{T_{die} - T_a}\right)\right]^2} \tag{37}$$

where θ is the number of calculated points, $T_{B_f,k}(\bar{x})$ and $T_{HTC_{total},k}(\bar{x})$ represent calculated temperature of the film at a given dimensionless drawing distance $\bar{x}$ using full (i.e. using a given value of B_f in Eq. (24)) and simplified (i.e. using a given value of HTC_{total} in Eq. (22)) model, respectively, T_{die} is the film temperature at the die exit and T_a is the air temperature. Equivalent constant HTC_{total} for given B_f was determined for the case in which $nRMSE_{B_f}$ was minimum.

The parametric study using the EFC model accounting for flow-induced crystallization was performed for reference processing conditions marked as Ab1 in Table 3. Model predictions for film temperature and crystallinity as a function of dimensionless drawing distance considering full model using different B_f values are shown in Fig. 7a-b. If the cooling intensity is low, the temperature of the film decreases slightly, and the final crystallinity is zero ($0 < B_f < 0.5$). With increasing cooling intensity ($B_f > 0.5$), the lowering of the film temperature is intense and the polymer melt begins to crystallize, which is indicated in the temperature profile by the appearance of a region with a slightly decreasing or even slightly increasing temperature due to the exothermic na-

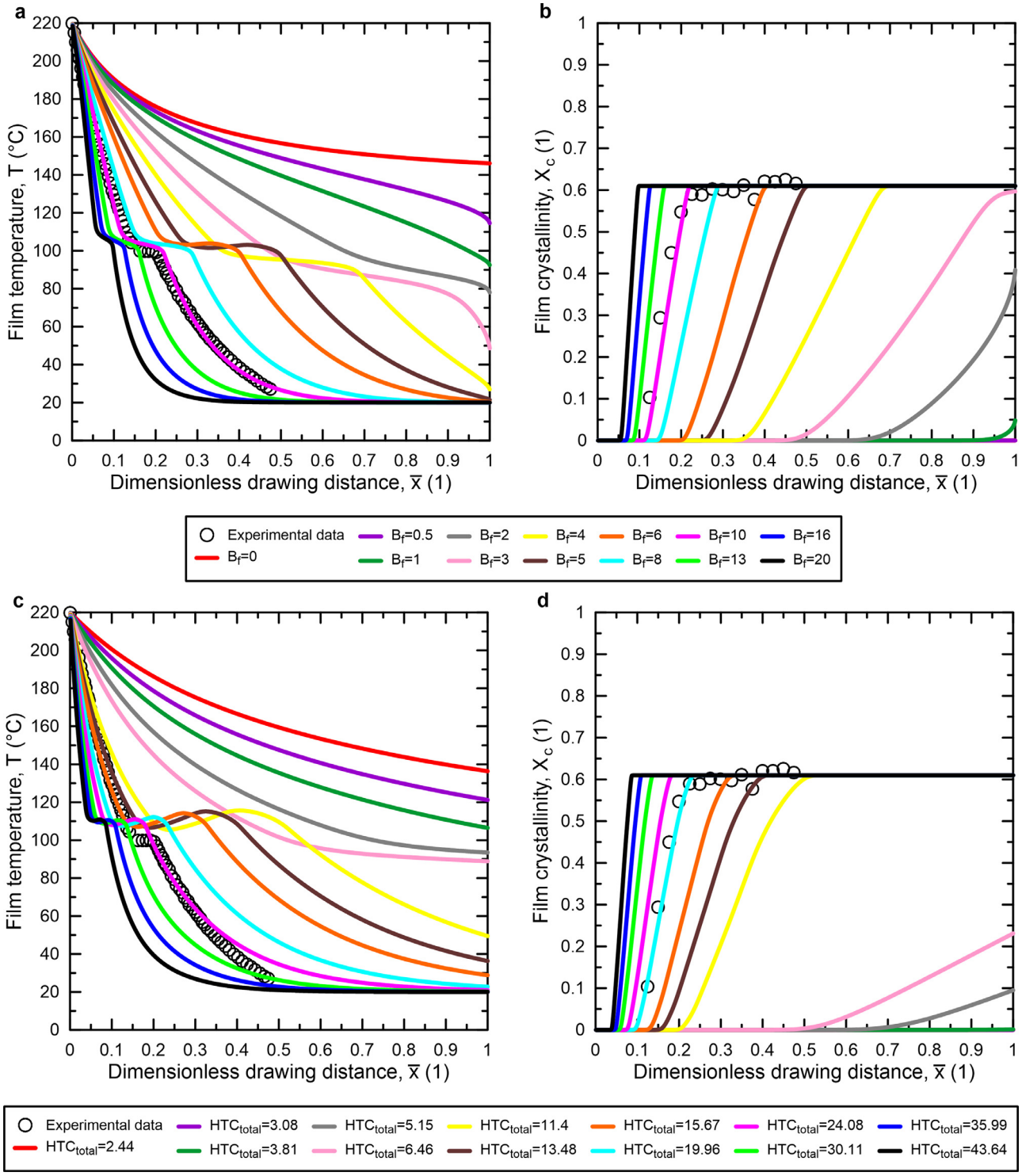

Fig. 7. Model predicted effect of HTC on film temperature and crystallinity (model accounting for flow-induced crystallization) as a function of dimensionless drawing distance using full model that uses a variable HTC given by Eq. (23) (by changing parameter B_f in forced convection term appearing in Eq. (24)) [(a) and (b)] or by using simplified model that uses an equivalent constant HTC_{total} value [(c) and (d)]. Process conditions are summarized in Table 3 (marked as Ab1). Units: B_f (1), HTC_{total} ($J \cdot s^{-1} \cdot K^{-1} \cdot m^{-2}$).

ture of crystallization (see Fig. 7a). The crystallinity profiles for the given B_f values are shown in Fig. 7b. It can be seen that the movement of the crystallization onset from the chill roll region to the die region with an increased B_f value is relatively smooth.

The film temperature profiles obtained in the previous step for the given B_f values were fitted using the simplified model. In this way, it was possible to determine a equivalent constant value of the HTC_{total} for the given B_f value. The best fits of the simplified model for the temperature profiles and the corresponding predictions for crystallinity are shown in Fig. 7c-d. Comparing Fig. 7a-b and Fig. 7c-d, it can be seen that the ability of the simplified model to describe the temperature profiles obtained using the variable-

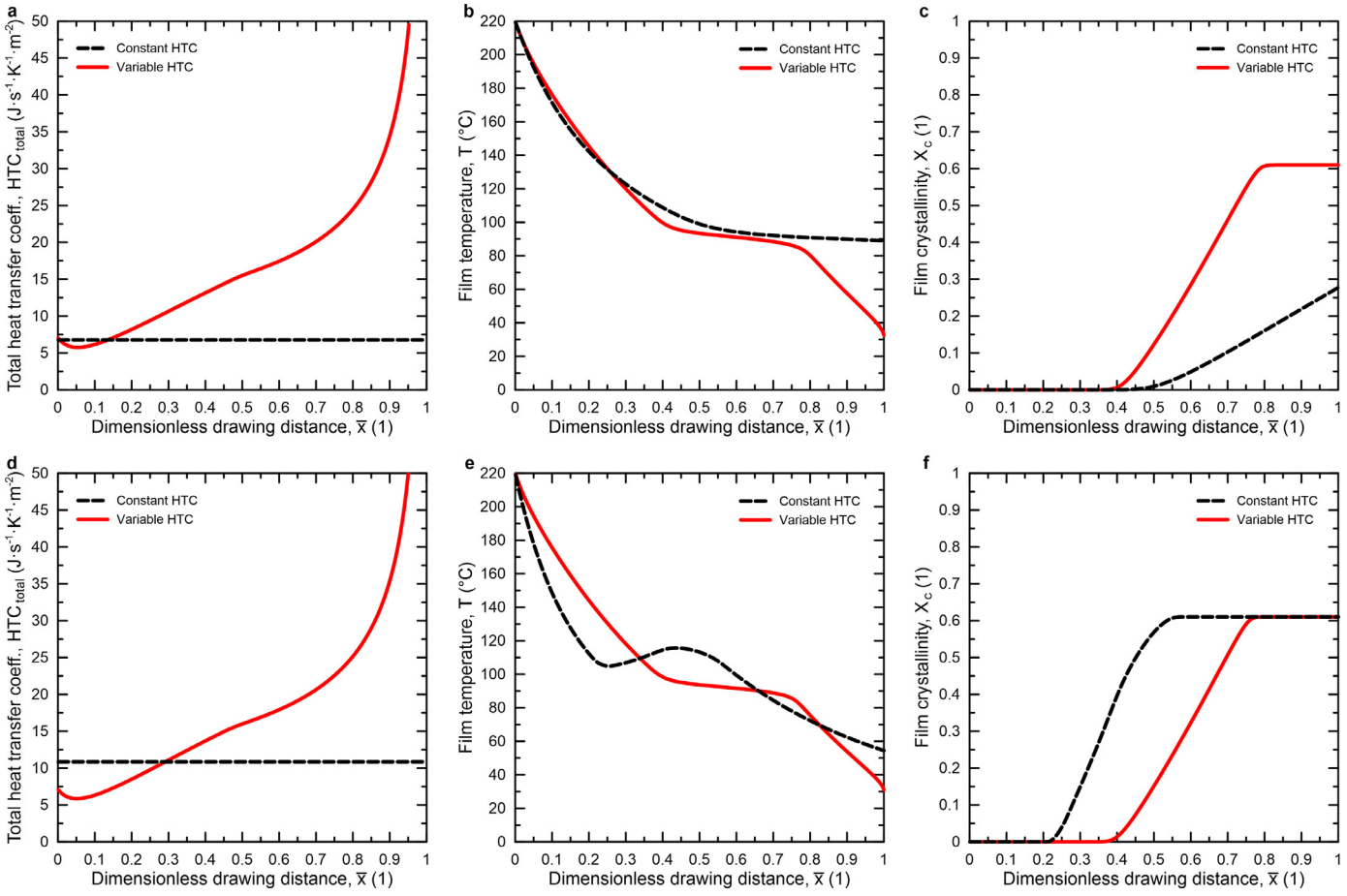

Fig. 8. Comparison between full and simplified model predictions (both models accounting for flow-induced crystallization) just below [B_f=3.6, HTC_{total}=6.78 J·s^{-1}·K^{-1}·m^{-2}, (a)-(c)] and just above [B_f=3.7, HTC_{total}=10.85 J·s^{-1}·K^{-1}·m^{-2} (d)-(f)] development of HTC_{total} [(a), (d)], temperature [(b), (e)] and crystallinity across the air-gap [(c), (f)]. Process conditions are summarized in Table 3 (marked as Ab1).

HTC-based model has its limits. The simplified model begins to over predict the intensity of the flow-induced crystallization under moderate cooling conditions (see pronounced local maxima in the calculated temperature profiles provided in Fig. 7c caused by the predicted artificially high amount of exothermic heat). It can be seen in Fig. 7d that the predicted movement of the crystallization onset from the chill roll region to the die region with the increasing HTC_{total} value has an abrupt character at the moderate values of HTC_{total}. An abrupt change in the behavior of the simplified model occurs when the B_f values in the full model change from 3.6 to 3.7 for the given processing conditions, as shown in Fig. 8.

For the case, in which $B_f = 3.6$, (see Fig. 8a-c) the simplified model gives an equivalent constant value of $HTC_{total} = 6.78\ \mathrm{J \cdot s^{-1} \cdot K^{-1} \cdot m^{-2}}$ ($nRMSE_{B_f} = 0.081$). This leads to a reasonable description of the film temperature at a dimensionless drawing distance $0 \leq \bar{x} \leq 0.2$, where the HTC values, i.e. the cooling efficiency, of the two models are comparable. When $\bar{x} > 0.2$, the cooling efficiency increases in the full model, which initiates and promotes the flow-induced crystallization at $\bar{x} = 0.4$, which generates the exothermic heat that is effectively removed from the film because the cooling efficiency is high. The film temperature thus becomes predicted by the full model practically constant from $\bar{x} = 0.4$ approximately to $\bar{x} = 0.8$. The simplified model is able to describe this temperature plateau region also quite well, but the mechanism behind it is different compared to the full model. Since it uses a smaller value of HTC compared to the full model, the onset of flow-induced crystallization is delayed to about $\bar{x} = 0.5$, its intensity is reduced, and thus a correspondingly small amount of generated exothermic heat can be effectively removed from the film (up to about $\bar{x} = 0.8$), although in this case the cooling efficiency is low. If $\bar{x} > 0.8$, the full and simplified model predictions differ. At these locations, the full model predicts that the film is fully crystalized, and no exothermic heat generation occurs. Since the full model provides the highest HTC value in these locations, the film temperature is significantly reduced here. The simplified model predicts the continued occurrence of the crystallization process with subsequent exothermal heat generation in these locations. As the HTC value remains constant (much lower compared to the full model), the cooling efficiency is not high enough to release a large enough amount of heat from the film to lower its temperature. Compared to the full model, the simplified model thus predicts a higher final film temperature and a lower final film crystallinity.

For the case in which B_f was slightly increased from 3.6 to 3.7, (see Fig. 8d-f), the simplified model greatly increased the equivalent constant value of HTC, from $6.78\ \mathrm{J \cdot s^{-1} \cdot K^{-1} \cdot m^{-2}}$ to $10.85\ \mathrm{J \cdot s^{-1} \cdot K^{-1} \cdot m^{-2}}$ ($nRMSE_{B_f} = 0.085$). While the behavior of the full model is virtually unchanged, the behavior of the simplified model changed significantly. The cooling intensity of the simplified model is now much higher than that of the full model at about $0 \leq \bar{x} \leq 0.3$, leading to underprediction of melt temperature, early onset of flow-induced crystallization, and generation of cor-

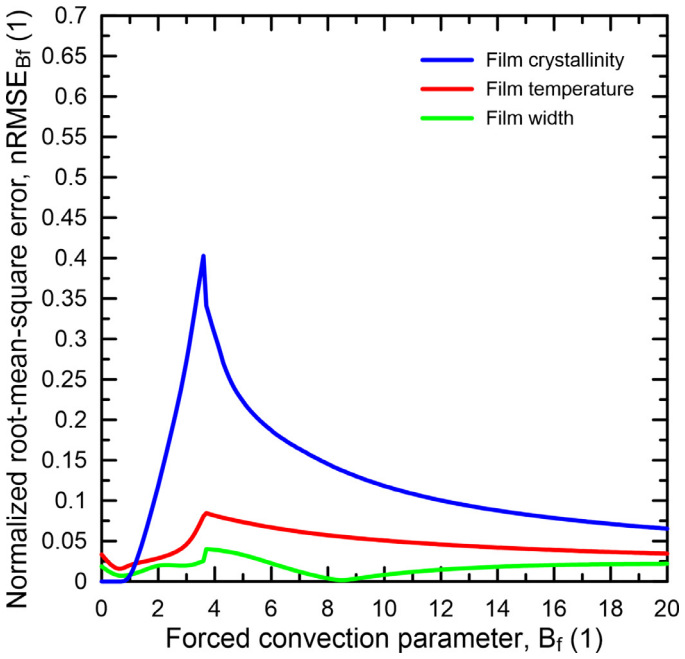

Fig. 9. Differences between full and simplified model predictions (both models account for flow-induced crystallization) expressed by the normalized root-mean-square error, $nRMSE_{Bf}$ (Eq. (37)) calculated over the air-gap for film temperature, crystallinity, and film half-width, plotted as a function of the force convection parameter B_f. Process conditions are summarized in Table 3 (marked as Ab1).

responding exothermic heat. For $\bar{x} > 0.3$, the cooling efficiency of the simplified model has decreased compared to the full model because there is not a high enough heat removal, so the film temperature even rises, reaches a maximum, and then decreases. This drop in temperature is possible because the film has prematurely fully crystallized at about $\bar{x} = 0.6$, i.e. no further exothermic heat evolution occurs and the given cooling intensity is high enough to reduce the film temperature in the region of the cooling roll. Since the cooling efficiency is lower in this region for the simplified model than for the full model, the film temperature drop is weak. Thus, compared to the full model, the simplified model predicts a higher final film temperature and the same final film crystallinity (i.e. fully crystallized film).

The Fig. 9 provides $nRMSE_{B_f}$ to quantify the degree of difference between full and simplified model predictions along the dimensionless drawing distance for a wide range of cooling intensities (i.e. for different values of B_f and equivalent constant values of HTC_{total}) with respect to temperature (using Eq. (37)), crystallinity (via Eq. (37) using actual to equilibrium crystallinity ratio) and film half-width (via Eq. (37) using the actual to extrusion die half-width ratio). It can be seen that the $nRMSE_{B_f}$ is lowest for film width. For crystallinity and film temperature, the $nRMSE_{B_f}$ is low, then increases to a certain maximum and then decreases with increased cooling efficiency. This suggests, that using a simplified model to predict film temperature, crystallinity, and film half-width can only be reliable under very low or very high cooling conditions. It can be seen even more clearly in Figs. 10 and 11 where $nRMSE_{B_f}(\bar{x} = X)$, or exact value for the final monitored variables (i.e. at the chill roll where $\bar{x} = X$) are provided. It can be seen that the simplified model tends to underpredict the final crystallinity and overpredict final film temperature at all cooling rates, where the predictions of the two model differ significantly. On the other hand, the stress generated in the produced film, which has strong impact on the final film mechanical properties, as shown in [98], appears to be reliably predicted by the simplified model only at very low cooling intensities, because the differences in the model prediction for the drawing force are very small (see Fig. 10b). At the higher cooling intensities (i.e. if $B_f >$ 3.6 in this case), the deviation between the full and simplified model increases monotonically with increased cooling efficiency, as the simplified model tends to overpredict the take-up force (see Fig. 11b).

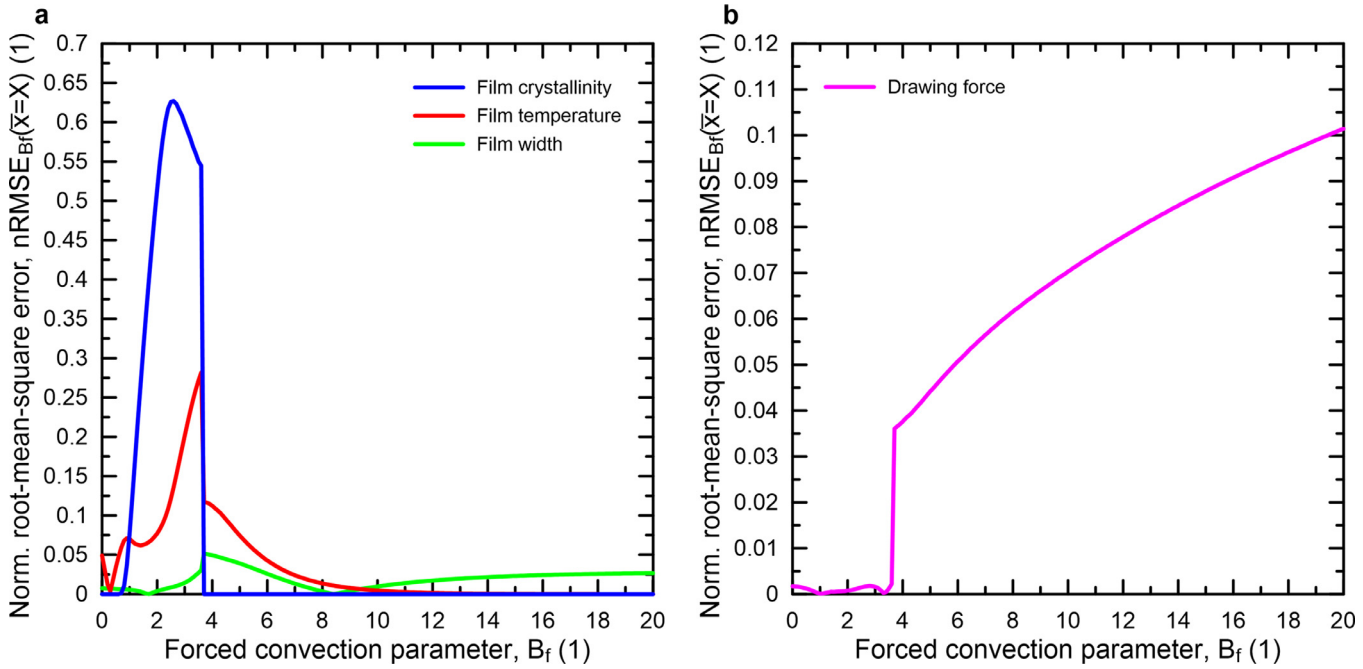

Fig. 10. Differences between full and simplified model predictions (both models account for flow-induced crystallization) expressed by the normalized root-mean-square error, $nRMSE_{B_f}$ at the chill roll (using Eq. (37) where $\bar{x} = X$) for film temperature (a), crystallinity (a), film half-width (a) and drawing force (b), plotted as a function of the forced convection parameter B_f. Process conditions are summarized in Table 3 (marked as Ab1).

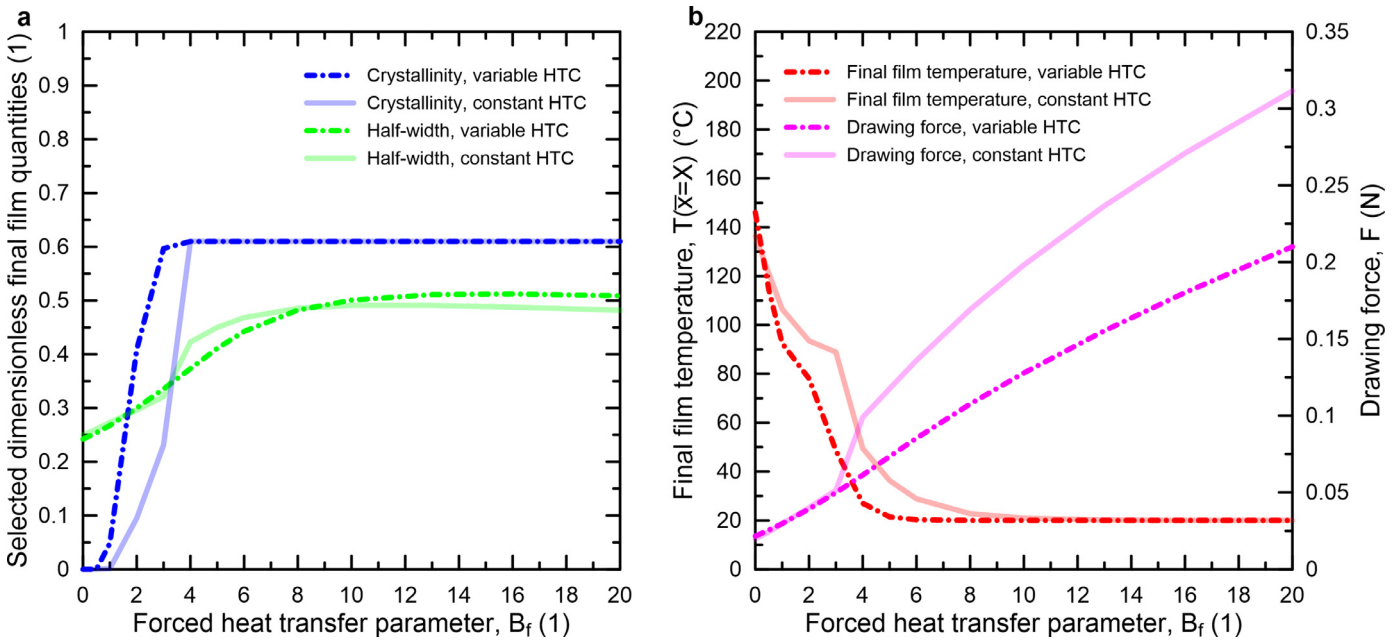

Fig. 11. Comparison between full and simplified model predictions (both models accounting for flow-induced crystallization) at the chill roll for crystallinity (a), film half-width (a) and film temperature (b) and drawing force (b), plotted as a function of the forced convection parameter B_f. Process conditions are summarized in Table 3 (marked as Ab1).

4. Conclusions

In this work, the recently proposed viscoelastic non-isothermal EFC model, which accounts for flow-induced crystallization, was generalized by including HTC considering radiation, natural and forced convection. This variable-HTC-based model was found to have the ability to predict the measured temperature, velocity, width and crystallization profile for process conditions typical for the production of PP energy storage membranes, as it can handle low and high (i.e., different) cooling intensities at the die exit and the chill roll region, respectively. On the other hand, it was found that the model based on constant HTC underestimates the temperature in the die exit region, which promotes flow-induced crystallization and the generation of exothermic heat causing the formation of an artificial local maximum in the temperature profile, and thus the temperature at the chill roll is overestimated due to insufficient cooling intensity. After switching off flow-induced crystallization, none of the tested models was able to describe the temperature and crystallinity of the film.

The difference between variable and constant HTC based models was investigated in more details by using systematic parametric study. It was revealed that the model based on constant HTC can reliably predict the final film temperature, crystallinity, and film half-width only under very low or very high cooling conditions. On the other hand, it appears that the stress generated in the produced film, which has a strong impact on the final mechanical properties of the film, is reliably predicted by the simplified model only at very low cooling intensities. At higher cooling intensities, the deviation between the variable-HTC model and the constant-HTC model increases monotonically with increased cooling efficiency, as the variable-HTC model tends to overpredict the take-up force. This suggests that the use of the variable-HTC model should be preferred for polymer energy membrane production over the constant-HTC models, and flow-induced crystallization should always be included, otherwise the EFC model does not represent the experimental reality.

It is believed that the proposed model and the obtained results can help to understand the optimal process conditions for the production of polymer membranes for energy storage due to their use in rechargeable lithium-ion batteries and special energy storage.

Declaration of Competing Interest

The authors declare that they have no known competing financial interests or personal relationships that could have appeared to influence the work reported in this paper.

CRediT authorship contribution statement

Tomas Barborik: Formal analysis, Investigation, Methodology, Visualization, Writing – original draft, Writing – review & editing. **Martin Zatloukal:** Conceptualization, Formal analysis, Investigation, Methodology, Writing – original draft, Writing – review & editing.

Data availability

Data will be made available on request.

Acknowledgments

The authors wish to acknowledge the Grant Agency of the Czech Republic (Grant No. 21–09174S) for the financial support.

References

[1] J. Kang, D.-Y. Han, S. Kim, J. Ryu, S. Park, Multiscale polymeric materials for advanced lithium battery applications, Adv. Mater. 35 (4) (2023).
[2] Z. Zou, Z. Hu, H. Pu, Lithium-ion battery separators based-on nanolayer co-extrusion prepared polypropylene nanobelts reinforced cellulose, J. Memb. Sci. 666 (2023).
[3] M.H. Moghim, A. Nahvibayani, R. Eqra, Mechanical properties of heat-treated polypropylene separators for Lithium-ion batteries, Polym. Eng. Sci. 62 (9) (2022) 3049.
[4] Y. Qiu, F. Jiang, A review on passive and active strategies of enhancing the safety of lithium-ion batteries, Int. J. Heat Mass Transf. 184 (2022).
[5] J. Choi, P.J. Kim, A roadmap of battery separator development: past and future, Curr. Opin. Electrochem. 31 (2022) 100858.

[6] F. Wang, X. Ke, K. Shen, L. Zhu, C. Yuan, A critical review on materials and fabrications of thermally stable separators for lithium-ion batteries, Adv. Mater. Technol. 7 (5) (2022).
[7] L. Ding, D. Li, F. Du, D. Zhang, S. Zhang, R. Xu, T. Wu, Fabrication of Nano-Al2O3 in-situ coating lithium-ion battery separator based on synchronous biaxial stretching mechanism of β-crystal polypropylene, Ind. Eng. Chem. Res. 61 (30) (2022) 11034.
[8] W. Luo, S. Cheng, M. Wu, X. Zhang, D. Yang, X. Rui, A review of advanced separators for rechargeable batteries, J. Power Sources 509 (2021).
[9] M.K. Purkait, M.K. Sinha, P. Mondal, R. Singh, Stimuli Responsive Polymeric Membranes: Smart Polymeric Membranes, An Imprint of Elsevier, London, 2018. https://www.books.google.cz/books?id=fE0vswEACAAJ. ISBN: 0128139617, 9780128139615.
[10] Y.L. Yeow, On the stability of extending films: a model for the film casting process, J. Fluid Mech. 66 (3) (1974) 613.
[11] G.R. Aird, Y.L. Yeow, Stability of film casting of power-law liquids, Ind. Eng. Chem. Fundam. 22 (1) (1983) 7.
[12] N.D. Polychronopoulos, T.D. Papathanasiou, A study on the effect of drawing on extrudate swell in film casting, Appl. Rheol. 25 (4) (2015) 1.
[13] M. Bechert, Non-Newtonian effects on draw resonance in film casting, J. Nonnewton. Fluid Mech. 279 (2020) 104262.
[14] J.F. Agassant, P. Avenas, J.P. Sergent, P.J. Carreau, Polymer Processing: Principles and Modeling, Hanser Gardner Publications, 1991. https://books.google.ca/books?id=BgPqGwAACAAJ. ISBN: 1569900000, 9781569900000.
[15] D. Silagy, Y. Demay, J.F. Agassant, Study of the stability of the film casting process, Polym. Eng. Sci. 36 (21) (1996) 2614.
[16] Y. Kwon, One-dimensional modeling of flat sheet casting or rectangular fiber spinning process and the effect of normal stresses, Korea-Australia Rheol. J. 11 (3) (1999) 225.
[17] H. Ito, M. Doi, T. Isaki, M. Takeo, A model of neck-in phenomenon in film casting process, J. Soc. Rheol. Japan 31 (3) (2003) 157.
[18] S. Bourrigaud, G. Marin, V. Dabas, C. Dupuy, D. Silagy, The draw ratio–Deborah number diagram: a useful tool for coating applications, Polym. Eng. Sci. 46 (3) (2006) 372.
[19] H.V. Pol, S.S. Thete, P. Doshi, A.K. Lele, Necking in extrusion film casting: the role of macromolecular architecture, J. Rheol. 57 (2) (2013) 559.
[20] M. Bechert, D.W. Schubert, B. Scheid, On the stabilizing effects of neck-in, gravity, and inertia in Newtonian film casting, Phys. Fluids 28 (2) (2016) 024109.
[21] H.V. Pol, S.S. Thete, Necking in extrusion film casting: numerical predictions of the maxwell model and comparison with experiments, J. Macromol. Sci. Part B 55 (10) (2016) 984.
[22] N.R. Anturkar, A. Co, Draw resonance in film casting of viscoelastic fluids: a linear stability analysis, J. Nonnewton. Fluid Mech. 28 (3) (1988) 287.
[23] T. Barborik, M. Zatloukal, C. Tzoganakis, On the role of extensional rheology and Deborah number on the neck-in phenomenon during flat film casting, Int. J. Heat Mass Transf. 111 (2017) 1296.
[24] R. Dhadwal, S. Banik, P. Doshi, H.V. Pol, Effect of viscoelastic relaxation modes on stability of extrusion film casting process modeled using multimode Phan-Thien-Tanner constitutive equation, Appl. Math. Model. 47 (2017) 487.
[25] S.S. Thete, P. Doshi, H.V. Pol, New insights into the use of multi-mode phenomenological constitutive equations to model extrusion film casting process, J. Plast. Film Sheeting 33 (1) (2017) 35.
[26] T. Barborik, M. Zatloukal, Effect of die exit stress state, Deborah number, uniaxial and planar extensional rheology on the neck-in phenomenon in polymeric flat film production, J. Nonnewton. Fluid Mech. 255 (2018) 39.
[27] S. D'Halewyu, J.F. Agassant, Y. Demay, Numerical simulation of the cast film process, Polym. Eng. Sci. 30 (6) (1990) 335.
[28] B. Debbaut, J.M. Marchal, M.J. Crochet, in: J. Casey, M.J. Crochet (Eds.), Theoretical, Experimental, and Numerical Contributions to the Mechanics of Fluids and Solids, 46, 1995, pp. 679–698. https://www.scopus.com/inward/record.uri?eid=2-s2.0-0000893517&partnerID=40&md5=68ff62d4ca22e05b119e860d53dce816.
[29] D. Silagy, Y. Demay, J.F. Agassant, Stationary and stability analysis of the film casting process, J. Nonnewton. Fluid Mech. 79 (2–3) (1998) 563.
[30] D. Silagy, Y. Demay, J.F. Agassant, Numerical simulation of the film casting process, Int. J. Numer. Methods Fluids 30 (1) (1999) 1.
[31] K. Christodoulou, S.G. Hatzikiriakos, D. Vlassopoulos, Stability analysis of film casting for PET resins using a multimode Phan-Thien-Tanner constitutive equation, J. Plast. Film Sheeting 16 (4) (2000) 312.
[32] T. Kajiwara, M. Yamamura, T. Asahina, Relationship between neck-in phenomena and rheological properties in film casting, Nihon Reoroji Gakkaishi 34 (2) (2006) 97.
[33] P. Barq, J.M. Haudin, J.F. Agassant, H. Roth, P. Bourgin, Instability phenomena in film casting process, Int. Polym. Proc. 5 (4) (1990) 264.
[34] H. Kometani, T. Matsumura, T. Suga, T. Kanai, Experimental and theoretical analyses of film casting process, J. Polym. Eng. 27 (1) (2007) 1.
[35] J.S. Lee, J.M. Kim, Effect of aspect ratio and fluid elasticity on chain orientation in isothermal film casting process, Korean J. Chem. Eng. 27 (2) (2010) 409.
[36] K. Sakaki, R. Katsumoto, T. Kajiwara, K. Funatsu, Three-dimensional flow simulation of a film-casting process, Polym. Eng. Sci. 36 (13) (1996) 1821.
[37] H. Zheng, W. Yu, C. Zhou, H. Zhang, Three dimensional simulation of viscoelastic polymer melts flow in a cast film process, Fibers Polym 8 (1) (2007) 50.
[38] V.R. Iyengar, A. Co, Film casting of a modified Giesekus fluid: a steady-state analysis, J. Nonnewton. Fluid Mech. 48 (1–2) (1993) 1.
[39] P. Barq, J.M. Haudin, J.F. Agassant, P. Bourgin, Stationary and dynamic analysis of film casting process, Int. Polym. Process. 9 (4) (1994) 350.
[40] V.R. Iyengar, A. Co, Film casting of a modified Giesekus fluid: stability analysis, Chem. Eng. Sci. 51 (9) (1996) 1417.
[41] M.E. Pis-Lopez, A. Co, Multilayer film casting of modified Giesekus fluids Part 1. Steady-state analysis, J. Nonnewton. Fluid Mech. 66 (1) (1996) 71.
[42] S. Smith, D.F.E. Stolle, Draw resonance in film casting as a response problem using a material description of motion, J. Plast. Film Sheeting 16 (2) (2000) 95.
[43] S. Smith, D. Stolle, A comparison of Eulerian and updated Lagrangian finite element algorithms for simulating film casting, Finite Elem. Anal. Des. 38 (5) (2002) 401.
[44] W. Minoshima, J.L. White, Stability of continuous film extrusion processes, J. Polym. Eng. 2 (3) (1983) 211.
[45] S.M. Alaie, T.C. Papanastasiou, Film casting of viscoelastic liquid, Polym. Eng. Sci. 31 (2) (1991) 67.
[46] G. Lamberti, G. Titomanlio, Analysis of film casting process: the heat transfer phenomena, Chem. Eng. Process. Process Intensif. 44 (10) (2005) 1117.
[47] G. Barot, I.J. Rao, Modeling the film casting process using a continuum model for crystallization in polymers, Int. J. Non. Linear. Mech. 40 (7) (2005) 939.
[48] H.V. Pol, S. Banik, L.B. Azad, S.S. Thete, P. Doshi, A. Lele, Nonisothermal analysis of extrusion film casting process using molecular constitutive equations, Rheol. Acta 53 (1) (2014) 85.
[49] K. Chikhalikar, S. Banik, L.B. Azad, K. Jadhav, S. Mahajan, Z. Ahmad, S. Kulkarni, S. Gupta, P. Doshi, H.V. Pol, A. Lele, Extrusion film casting of long chain branched polypropylene, Polym. Eng. Sci. 55 (9) (2015) 1977.
[50] Y.-G. Zhou, W.-B. Wu, J. Zou, L.-S. Turng, Dual-scale modeling and simulation of film casting of isotactic polypropylene, J. Plast. Film Sheeting 32 (3) (2016) 239.
[51] T. Barborik, M. Zatloukal, Effect of heat transfer coefficient, draw ratio and die exit temperature on the production of flat polypropylene membranes, Phys. Fluids 31 (5) (2019) 053101.
[52] W.S. Smith, Nonisothermal Film Casting of a Viscous Fluid, Ph.D. Thesis, McMaster University, 1997 Available at:http://www.cas.mcmaster.ca/~smiths/Masters_abstract.html.
[53] S. Smith, D. Stolle, Nonisothermal two-dimensional film casting of a viscous polymer, Polym. Eng. Sci. 40 (8) (2000) 1870.
[54] N. Satoh, H. Tomiyama, T. Kajiwara, Viscoelastic simulation of film casting process for a polymer melt, Polym. Eng. Sci. 41 (9) (2001) 1564.
[55] W.S. Smith, Simulating the Cast Film Process Using an Updated Lagrangian Finite Element Algorithm, Ph.D. Thesis, McMaster University, 2001 Available at:http://www.cas.mcmaster.ca/~smiths/PhD_abstract.html.
[56] D. Cotto, P. Duffo, J.M. Haudin, Cast film extrusion of polypropylene films, Int. Polym. Process. 4 (2) (1989) 103.
[57] S. Smith, D. Stolle, Numerical simulation of film casting using an updated lagrangian finite element algorithm, Polym. Eng. Sci. 43 (5) (2003) 1105.
[58] C. Sollogoub, Y. Demay, J.F. Agassant, Cast film problem: a non isothermal investigation, Int. Polym. Process. 18 (1) (2003) 80.
[59] C. Sollogoub, Y. Demay, J.F. Agassant, Non-isothermal viscoelastic numerical model of the cast-film process, J. Nonnewton. Fluid Mech. 138 (2–3) (2006) 76.
[60] K. Aniunoh, An Experimental and Numerical Study of the Film Casting Process, Ph.D. Thesis, Clemson University, 2007 Available at:https://tigerprints.clemson.edu/all_dissertations/148/.
[61] D.M. Shin, J.S. Lee, J.M. Kim, H.W. Jung, J.C. Hyun, Transient and steady-state solutions of 2D viscoelastic nonisothermal simulation model of film casting process via finite element method, J. Rheol. 51 (3) (2007) 393.
[62] S. Shiromoto, Y. Masutani, M. Tsutsubuchi, Y. Togawa, T. Kajiwara, A neck-in model in extrusion lamination process, Polym. Eng. Sci. 50 (1) (2010) 22.
[63] S. Shiromoto, Y. Masutani, M. Tsutsubuchi, Y. Togawa, T. Kajiwara, The effect of viscoelasticity on the extrusion drawing in film-casting process, Rheol. Acta 49 (7) (2010) 757.
[64] S. Shiromoto, The mechanism of neck-in phenomenon in film casting process, Int. Polym. Process. 29 (2) (2014) 197.
[65] Y. Mu, L. Hang, G. Zhao, X. Wang, Y. Zhou, Z. Cheng, Modeling and simulation for the investigation of polymer film casting process using finite element method, Math. Comput. Simul. 169 (2020) 88.
[66] H. Zheng, W. Yu, C. Zhou, H. Zhang, Three-dimensional simulation of the non-isothermal cast film process of polymer melts, J. Polym. Res. 13 (6) (2006) 433.
[67] P. Duffo, B. Monasse, J.-M. Haudin, Influence of stretching and cooling conditions in cast film extrusion of PP films, Int. Polym. Process. 5 (1990) 272.
[68] P. Duffo, B. Monasse, J.M. Haudin, Cast film extrusion of polypropylene. Thermomechanical and physical aspects, J. Polym. Eng. 10 (1–3) (1991) 151.
[69] P. Barq, J.M. Haudin, J.F. Agassant, Isothermal and anisothermal models for cast film extrusion, Int. Polym. Process. 7 (4) (1992) 334.
[70] M. Beaulne, E. Mitsoulis, Numerical simulation of the film casting process, Int. Polym. Process. 14 (3) (1999) 261.
[71] D. Acierno, L. Di Maio, C.C. Ammirati, Film casting of polyethylene terephthalate: experiments and model comparisons, Polym. Eng. Sci. 40 (1) (2000) 108.
[72] G. Lamberti, G. Titomanlio, V. Brucato, Measurement and modelling of the film casting process 1. Width distribution along draw direction, Chem. Eng. Sci. 56 (20) (2001) 5749.

[73] G. Lamberti, G. Titomanlio, V. Brucato, Measurement and modelling of the film casting process: 2. Temperature distribution along draw direction, Chem. Eng. Sci. 57 (11) (2002) 1993.
[74] T. Barborik, M. Zatloukal, Viscoelastic non-isothermal modeling of film extrusion for membrane production including flow induced crystallization, Phys. Fluids 34 (2022) 063103.
[75] N. Billon, P. Barq, J.M. Haudin, Modelling of the cooling of semi-crystalline polymers during their processing, Int. Polym. Process. 6 (4) (1991) 348.
[76] J.M. Coulson, J.F. Richardson, Coulson & Richardson's Chemical Engineering, Elsevier, Butterworth-Heinemann, Amsterdam, 1999. https://www.shop.elsevier.com/books/chemical-engineering-volume-1/chhabra/978-0-08-050101-7ISBN: 978-0-7506-4444-0
[77] T. Barborik, M. Zatloukal, Steady-state modeling of extrusion cast film process, neck-in phenomenon, and related experimental research: a review, Phys. Fluids 32 (6) (2020) 061302.
[78] O.S. Narayanaswamy, A one-dimensional model of stretching float glass, J. Am. Ceram. Soc. 60 (1–2) (1977) 1.
[79] A.I. Leonov, Nonequilibrium thermodynamics and rheology of viscoelastic polymer media, Rheol. Acta 15 (2) (1976) 85.
[80] A.I. Leonov, E.H. Lipkina, E.D. Paskhin, A.N. Prokunin, Theoretical and experimental investigation of shearing in elastic polymer liquids, Rheol. Acta 15 (7) (1976) 411.
[81] A.I. Leonov, A.N. Prokunin, An improved simple version of a nonlinear theory of elasto-viscous polymer media, Rheol. Acta 19 (4) (1980) 393.
[82] A.I. Leonov, A.N. Prokunin, On nonlinear effects in the extensional flow of polymeric liquids, Rheol. Acta 22 (2) (1983) 137.
[83] M. Simhambhatla, A.I. Leonov, On the rheological modeling of viscoelastic polymer liquids with stable constitutive equations, Rheol. Acta 34 (3) (1995) 259.
[84] A.I. Leonov, Constitutive equations for viscoelastic liquids: formulation, analysis and comparison with data, Rheol. Ser. 8 (C) (1999) 519.
[85] A.P. Kotula, K.B. Migler, Evaluating models for polycaprolactone crystallization via simultaneous rheology and Raman spectroscopy, J. Rheol. 62 (1) (2018) 343.
[86] R. Pantani, V. Speranza, G. Titomanlio, Simultaneous morphological and rheological measurements on polypropylene: effect of crystallinity on viscoelastic parameters, J. Rheol. 59 (2) (2015) 377.
[87] M. Zatloukal, Differential viscoelastic constitutive equations for polymer melts in steady shear and elongational flows, J. Nonnewton. Fluid Mech. 113 (2–3) (2003) 209, doi:10.1016/S0377-0257(03)00112-5.
[88] G. Titomanlio, V. Speranza, V. Brucato, On the simulation of thermoplastic injection moulding process: II Relevance of interaction between flow and crystallization, Int. Polym. Process. 12 (1) (1997) 45.
[89] R. Pantani, V. Speranza, G. Titomanlio, Evolution of iPP relaxation spectrum during crystallization, Macromol. Theory Simul. 23 (4) (2014) 300.
[90] R. Siegel, J.R. Howell, Thermal Radiation Heat Transfer, Hemisphere Pub. Corp., New York, 1981. https://www.books.google.cz/books/about/Thermal_Radiation_Heat_Transfer.html?hl=cs&id=wIEpAQAAMAAJ&redir_esc=y. ISBN: 0070573166, 9780070573161.
[91] A. Ziabicki, Crystallization of polymers in variable external conditions. 1. General equations, Colloid Polym. Sci. 274 (3) (1996) 209.
[92] A. Ziabicki, Crystallization of polymers in variable external conditions. II. Effects of cooling in the absence of stress and orientation, Colloid Polym. Sci. 274 (8) (1996) 705.
[93] G. Lamberti, G. Titomanlio, Crystallization kinetics of iPP. Model and experiments, Polym. Bull. 46 (2–3) (2001) 231.
[94] R. Pantani, F. De Santis, V. Speranza, G. Titomanlio, Analysis of flow induced crystallization through molecular stretch, Polymer 105 (2016) 187.
[95] G. Lamberti, G. Titomanlio, Analysis of film casting process : effect of cooling during the path in air, Ind. Eng. Chem. Res. 45 (2) (2006) 719.
[96] G. Lamberti, Flow-induced crystallization during isotactic polypropylene film casting, Polym. Eng. Sci. 51 (5) (2011) 851.
[97] E.A. Jensen, J.deC. Christiansen, Measurements of first and second normal stress differences in a polymer melt, J. Nonnewton. Fluid Mech. 148 (1–3) (2008) 41.
[98] R. Kolarik, M. Zatloukal, M. Martyn, The effect of polyolefin extensional rheology on non-isothermal film blowing process stability, Int. J. Heat Mass Transf. 56 (1–2) (2013) 694.
[99] M. Zatloukal, T. Barborik, in: Annual Technical Conference - ANTEC, Conference Proceedings 2019-March, Society of Plastics Engineers, Dallas, TX, 2019, p. 1597. https://www.scopus.com/inward/record.uri?eid=2-s2.0-85072973918&partnerID=40&md5=d2c2006677306310c304e07fe5ce84e0. ISBN: 978-171380198-6.
[100] S. Coppola, L. Balzano, E. Gioffredi, P.L. Maffettone, N. Grizzuti, Effects of the degree of undercooling on flow induced crystallization in polymer melts, Polymer 45 (10) (2004) 3249.
[101] G. Lamberti, G. Titomanlio, Evidences of flow induced crystallization during characterized film casting experiments, Macromol. Symp. 185 (1) (2002) 167.
[102] B. Ellis, R. Smith, in: Polymers: A Property Database, 2nd, Boca Raton, 2009, p. 1052, doi:10.1201/9781420005707.
[103] J.E. Mark, Physical Properties of Polymer Handbook, Springer, NY, New York, 2007, doi:10.1007/978-0-387-69002-5.
[104] M. Arroyo, M.A. Lopez-Manchado, F. Avalos, Crystallization kinetics of polypropylene: II. Effect of the addition of short glass fibres, Polymer (Guildf) 38 (22) (1997) 5587.